Dense molecular gas at 12 mm towards Galactic TeV gamma-ray sources

P. de Wilt,[1]★ G. Rowell,[1]★ A. J. Walsh,[2] M. Burton,[3,4] J. Rathborne,[5] Y. Fukui,[6] A. Kawamura[7] and F. Aharonian[8,9,10]

[1]*School of Physical Sciences, University of Adelaide, Adelaide, SA 5005, Australia*
[2]*International Centre for Radio Astronomy Research, Curtin University, Bentley, WA 6102, Australia*
[3]*School of Physics, University of New South Wales, Sydney, NSW 2052, Australia*
[4]*Armagh Observatory and Planetarium, College Hill, Armagh BT61 9DG, UK*
[5]*CSIRO Astronomy and Space Science, Marsfield, NSW 2122, Australia*
[6]*Department of Astrophysics, Nagoya University, Furocho, Chikusa-ku, Nagoya, Aichi 464-8602, Japan*
[7]*National Astronomical Observatory of Japan, 2-21-1 Osawa, Mitaka, Tokyo 181-8588, Japan*
[8]*Dublin Institute for Advanced Studies, School of Cosmic Physics, 31 Fitzwilliam Place, Dublin 2, Ireland*
[9]*Max Planck Institute for Nuclear Physics, Saupfercheckweg 1, D-69117 Heidelberg, Germany*
[10]*National Research Nuclear University (MEPHI), 115409 Moscow, Russia*

ABSTRACT

The High Energy Stereoscopic System has revealed many TeV (10^{12} eV) gamma-ray sources along the Galactic plane, and around 30 per cent of these sources remain unidentified. The morphology and dynamics of dense gas coincident and surrounding the gamma-ray emission can provide clues about the nature of the TeV emission. The H_2O Southern Galactic Plane Survey (HOPS) undertaken with the Mopra radio telescope includes several dense gas tracers, such as NH_3 (n,n) transitions and HC_3N (3–2), star formation tracers including H_2O masers and radio recombination lines that trace ionized gas. A search for dense gas, traced by NH_3 (1,1) emission seen in HOPS and additional observations, towards Galactic TeV sources has been undertaken. Of the 49 Galactic TeV sources covered by 12 mm observations, NH_3 (1,1) is detected towards or adjacent to 38 of them. Dense gas counterparts have been detected near several unidentified Galactic TeV sources that display morphology pointing to a hadronic origin to the TeV gamma-rays. The dense gas detected towards some TeV sources displays unusual emission characteristics, including very broad linewidths and enhanced ortho-to-para NH_3 abundance ratios towards HESS J1745−303 and HESS J1801−233, which reflects previous shock activity within the gas.

Key words: pulsars: general – ISM: clouds – cosmic rays – ISM: supernova remnants – gamma-rays: general – gamma-rays: ISM.

1 INTRODUCTION

The sensitivity of the current generation of ground-based Very High Energy (VHE) gamma-ray experiments such as the High Energy Stereoscopic System (HESS; de Oña Wilhelmi 2009) has led to the discovery of many previously unknown sources of TeV (10^{12} eV) gamma-rays towards the Galactic plane. The largest fraction of Galactic TeV gamma-ray sources is still made up of unidentified objects (Pühlhofer et al. 2015).

TeV gamma-rays are produced by interactions of relativistic particles and so their observation provides a probe of non-thermal astrophysical processes. GeV–TeV gamma-rays are produced hadronically, through proton–proton interactions, and/or leptonically, via inverse Compton (IC) scattering or bremsstrahlung. The presence of dense molecular gas can give clues about both leptonic and hadronic production of TeV gamma-rays.

The flux of gamma-rays that are produced hadronically, through proton–proton interactions, can be expected to peak along with the density of gas near proton accelerators. Coincident dense gas and TeV emission can be seen in sources such as HESS J1801−233 (see Aharonian et al. 2008b), a supernova remnant (SNR)/molecular cloud interaction region, to the NE of SNR W28, as well as parts of HESS J1745−303 (Aharonian et al. 2008c) and RX J1713.7−3946 (Maxted et al. 2012). TeV gamma-ray sources that are produced leptonically through IC emission, for example pulsar wind nebulae (PWNe), often exhibit asymmetric morphology. In the case of PWNe, this asymmetry may be explained by an inhomogeneous distribution of interstellar gas around pulsars that strongly

★ E-mail: phoebe.dewilt@gmail.com (PdeW); growell@physics.adelaide.edu.au (GR)

influences their development (e.g. Blondin, Chevalier & Frierson [2001]). The TeV emission then tails off in a direction away from the denser parts of the interstellar gas.

Star formation that may not show up as infrared (IR) sources may be traced by molecular transitions in the 12 mm band pass, such as H_2O masers (Walsh et al. [2011]). There is evidence that H_2O masers, signposts of outflows and shocked gas, may be observable at very early stages of star formation (e.g. Forster & Caswell [2000]). Ionized gas in H II regions is also traced by radio recombination lines such as H69α that is included in our study. This provides an opportunity to test what role star-forming regions play in TeV gamma-ray emission.

High-mass stars have been linked with TeV gamma-ray emission through particle acceleration in SNRs and PWNe. High-mass star-forming regions and/or young high-mass stellar objects may also have the potential to produce observable TeV gamma-ray emission through several mechanisms. The regions themselves could be sites of particle acceleration or the dense gas associated with these regions could simply provide target material for accelerate particles. Protostellar jets (which could be traced by H_2O masers) have been identified as potential sources of observable GeV gamma-rays (see Araudo & Rodríguez [2012]) where particles are accelerated at the jet termination shock (e.g. Bosch-Ramon et al. [2010]). Colliding wind binaries (CWBs) have been linked to TeV emission (e.g. Pittard & Dougherty [2006]; Bednarek & Pabich [2011]), but, so far, no CWB has been unambiguously associated with TeV gamma-rays and only one has been detected in GeV gamma-rays (Farnier, Walter & Leyder [2011]; Reitberger et al. [2015]). Wind-blown bubbles from high-mass stellar clusters and/or SNRs have long been proposed as sites of particle acceleration, through diffusive shock acceleration, up to PeV (10^{15} eV) energies (e.g. Casse & Paul [1980]) and recently, the first superbubble has been detected in TeV gamma-rays (H.E.S.S. Collaboration et al. [2015a]). Pedaletti, de Oña Wilhelmi & Torres ([2014]) show that regions of high stellar activity within the central Galactic region, traced by dust emission and CO, could be correlated with TeV emission.

In summary, dense molecular gas that is both coincident with and/or adjacent to TeV emission can be very important in identifying the TeV emission mechanism and the location of particle accelerators. The transitions included in this study can not only help understand the density profile of molecular clouds, but can also identify regions of unusual astrophysical conditions such as outflows (e.g. the H_2O maser), shocked gas (e.g. the H_2O maser and NH_3 transitions) and ionized gas (e.g. H69α). The kinematic velocity and linewidth of molecular transitions can provide information about the distance of and gas dynamics towards Galactic TeV gamma-ray sources.

Previously, the $^{12}CO(1–0)$ transition has been used to identify potential molecular cloud counterparts to unidentified TeV emission (e.g. Aharonian et al. [2008c]; Abramowski et al. [2011b]). For example, by making a thorough comparison of two Galactic plane data sets, the HESS TeV gamma-rays and the Nanten CO(1–0) emission, it was shown that the CO clouds in the W28 region have a remarkable spatial coincidence with the TeV gamma-rays (Aharonian et al. [2008b]). A subsequent comparative study towards the SNR RX J1713.7−3946 revealed that the combination of the atomic and molecular gas, i.e. the total interstellar hydrogen, shows a good spatial correspondence, where the Nanten CO $J = 1$–0 distribution and the ATCA H I 21 cm distribution were used to derive the gas column density (Fukui et al. [2012]). This correspondence is interpreted as indication for a hadronic component to the gamma-rays from RX J1713.7−3946 arising from the dense in-

terstellar medium (ISM) clumps (Zirakashvili & Aharonian [2010]; Inoue et al. [2012]). The interpretation is supported by the theoretical works on the VHE gamma-rays that incorporates the highly inhomogeneous distribution of the ISM (Inoue & Inutsuka [2012]; Gabici & Aharonian [2014]). Further observational identification of the molecular and atomic gas towards the VHE sources is presented by Fukuda et al. ([2014]) for HESS J1731−347, and Hayakawa et al. ([2012]) for HESS J1745−303. These observational and theoretical results indicate the important role of the ISM whose density is in a wide range from 10 to 10^5 cm^{-3} in producing the TeV gamma-rays, and warrant further systematic efforts to identify the interstellar gas towards the Galactic HESS sources.

While ^{12}CO is abundant, the $^{12}CO(1–0)$ transition has a critical density of $\sim$1000 cm^{-3} that contributes to the transition becoming optically thick towards molecular cloud cores. In addition, CO rapidly depletes from the gas phase towards the centre of cloud cores (e.g. see Bergin et al. [2002]; Tafalla et al. [2002]). Both of these aspects can hamper the understanding of molecular cloud density profiles and internal dynamics if the $^{12}CO(1–0)$ transition is used on its own. Due to the coarse angular resolution of current TeV observations ($\sim$0°.1), the Dame CO survey has been used to trace large-scale molecular content. As the angular and energy resolutions of TeV gamma-ray observations improve with the new generation of ground-based TeV telescope systems such as Cherenkov Telescope Array (CTA) (angular resolution 0°.02–0°.2), a better understanding of the density profiles of molecular clouds, using transitions that trace a wide range of temperatures and densities, will be needed to explore cosmic ray (CR) transport scenarios. Surveys such as Mopra CO (angular resolution $\sim$0°.01; Braiding et al. [2015]), Nanten2 (angular resolution $\sim$0°.03) and H_2O Southern Galactic Plane Survey (HOPS) (angular resolution $\sim$0°.03; Purcell et al. [2012]), used here, will be invaluable for this cause.

Ideal tracers of dense gases such as NH_3, CS or HC_3N are widely used to trace molecular cloud cores due to their lower abundance (a factor of $\sim$10^{-5} the CO abundance) and higher effective critical densities $\sim$10$^{4-5}$ cm^{-3}. This gives them much lower optical depths in dense gas and so allows for a more accurate calculation of gas density and mass towards dense ($\sim$10$^{4-5}$ cm^{-3}) molecular cloud cores. In addition, NH_3 depletes less rapidly than CO from the gas phase in cold molecular cloud cores (Tafalla et al. [2002]) and so is often used to trace cold ($<$30 K) gas that is often seen in infrared dark clouds (IRDCs). NH_3 inversion emission may be seen with collisional masers such as the H_2O maser traced in this study that is thought to trace protostellar jet termination shocks in early stages of star formation. The CS(1–0) and HC_3N transitions are used to trace warmer dense cores where star formation may already be switched on. These warmer cores are sometimes seen within H II regions, traced by radio recombination lines such as the H69α transition, where atomic hydrogen has been ionized by young, high-mass stars.

The NH_3 molecule is a pyramidal symmetric top with inversion motion and metastable levels, some of which display readily observable hyperfine structure. The NH_3 (1,1) transition displays prominent satellite lines, which along with NH_3 (2,2) allow the optical depth, and hence gas temperature and mass, to be strongly constrained (e.g. Ho & Townes [1983]; Walmsley & Ungerechts [1983]). NH_3 has two distinct species, distinguished by the relative nuclear spins of the hydrogen atoms, ortho NH_3 ($K = 3n$) in which all three spins are aligned and para NH_3 ($K \neq 3n$) in which the three spins are not aligned. The rotational temperature within the same spin species reflects the kinetic temperature under local thermodynamic equilibrium (LTE) conditions (Maret et al. [2009]). Since the transfer processes between ortho and para NH_3 are almost thermoneutral,

conversion between the two spin species is very slow with respect to the reactive pathways (which are exothermic). The time-scale of conversion processes between spin species is considered to be of the order of 10^6 yr in the gas phase (Cheung et al. 1969). As a result, the 'spin temperature' (or the rotational temperature between ortho and para species) is not considered to reflect the kinetic temperature of NH_3, but instead reflect formation conditions of the NH_3.

The ortho-to-para abundance ratio (OPR) for NH_3 is widely expected to be the statistical equilibrium value of 1.0 when the NH_3 molecules are formed in gas-phase or surface grain reactions (e.g. Umemoto et al. 1999). However, modelling by Faure et al. (2013) suggests that, in gas-phase reactions, the OPR can reasonably be expected to be 0.5–1.0, and an OPR < 1 reflects production from para-enriched H_2 gas. Faure et al. (2013) have modelled the formation of ortho and para ammonia and have suggested that ortho ammonia is formed preferentially over para ammonia when the NH_3 is formed or condensed on a cold surface (<30 K) such as water or ice. In addition, because the lowest energy level of the para species of NH_3 is 23 K higher than the lowest energy level of the ortho species, the para species require more energy for desorption than ortho species (Umemoto et al. 1999). Both of these aspects would enhance the OPR for NH_3 released from grain surfaces into the gas phase by shocks over the OPR of NH_3 produced in the gas phase. The observational study of Umemoto et al. (1999, amongst others) suggests that an enhanced OPR (OPR > 1) along with an enhanced NH_3 abundance can indicate a previous shock that has released NH_3 formed on dust grains into the gas phase.

This work provides a first systematic look at the dense gas ($n > 10^4$ cm^{-3}) traced by HOPS (Purcell et al. 2012) and further dedicated observations with the Mopra radio telescope towards Galactic TeV gamma-ray emission seen by HESS. The large (8 GHz) bandwidth of the Mopra spectrometer (MOPS) allows for the simultaneous observation of many molecular transitions. Multiple inversion–rotation transitions of NH_3 are included that allow us to identify molecular cloud cores displaying non-LTE conditions, which may indicate shocked gas. The velocity resolution (~0.4 km s^{-1} at 22 GHz; Urquhart et al. 2010) of MOPS at these wavelengths provides an opportunity to search for asymmetric line profiles of molecular transitions, which can indicate disruption and shocks within cloud cores. These Mopra observations are able to provide information about the densest parts of the interacting interstellar gas and will allow us to gain an insight in the CR penetration in the inner part of the cloud cores and the gamma-ray production.

2 OBSERVATIONS AND DATA REDUCTION

Our study uses published HESS results up to 2015 March (see Table 1 for specific references). HESS detects TeV gamma-rays above an energy threshold of ~100 GeV and up to ~100 TeV with a typical energy resolution of 15 per cent per photon and an angular resolution of ~0°.1 per event (Aharonian et al. 2006c). The HESS field of view is 5° in diameter with a point source sensitivity of ~2.0×10^{-13} erg cm^{-2} s^{-1} at 1 TeV (25 h obs).

Molecular line data were taken from HOPS (Walsh et al. 2011) data and reduced using the ATNF packages LIVEDATA, GRIDZILLA, ASAP and MIRIAD (see http://www.atnf.csiro.au/computing/software/ for information on these packages). HOPS has mapped a 100 square degree strip of the Galactic plane ($30° > l > -70°$, $|b| < 0°.5$) at 12 mm wavelengths using the Mopra radio telescope. The telescope main beam size (full width at half-maximum, FWHM) is ~2 arcmin at a wavelength of 12 mm (Urquhart et al. 2010). Mopra is a 22 m single-dish radio telescope located 450 km north-west of Sydney,

near Coonabarabran, NSW, Australia. HOPS observations made use of the MOPS in on-the-fly mapping mode. The zoom mode of MOPS allows simultaneous observations from up to 16 spectral windows, where each window is 137.5 MHz wide and contains 4096 channels. HOPS targets water masers, thermal molecular emission and radio recombination lines. Overlap of HOPS with the Galactic sky seen by HESS can be seen in Fig. 1. The Central Molecular Zone (CMZ) is not discussed in this study, and a study of this region will be detailed in a future paper. Further observation details of HOPS can be found described in Walsh et al. (2011). To derive kinematic distances from the local standard of rest (LSR) kinematic velocity, the Galactic rotation curve derived by Brand & Blitz (1993) was used unless otherwise indicated.

We also carried out dedicated observations with the Mopra radio telescope between 2011 February and 2015 January. These observations employed MOPS in zoom mode and utilized the same zoom bands and central frequency as HOPS. Five sites of deep ON/OFF pointing towards HESS J1801−233 and HESS J1745−303 were undertaken using modified zoom bands to include the NH_3 (4,4) and (5,5) transitions. Deep ON/OFF pointing is where one beam-sized 'ON' region is observed, and calibrated using a single, beam-sized 'OFF region and are used in this study to provide extra sensitivity over mapping data. The FWHM of the Mopra beam within the 12 mm band varies between 1.7 arcmin at the highest observed frequency in these data (27.5 GHz) and 2.4 arcmin at the lowest observed frequency (19.5 GHz; Urquhart et al. 2010). The mapping data, as with HOPS, use MOPS in on-the-fly mapping mode with two scanning directions, Galactic longitude and latitude, in order to reduce scanning artefacts and noise. Each 0°.5 × 0°.5 map took approximately 90 min for each pass. Deep ON/OFF pointings were undertaken for 60 min in selected regions where extra sensitivity was required. The mapping regions of our dedicated observations with HOPS-equivalent exposure have a mean T_{rms} of 0.2 K per channel. Mapping regions with deeper coverage had four times the exposure, and so achieved a T_{rms} ~0.1 K per channel. Position-switched deep ON/OFF observations achieved a T_{rms} of ≥~0.02 K per channel.

We applied the methods of Ungerechts, Winnewisser & Walmsley (1986) to estimate the NH_3 column density (N_{NH_3}), the kinetic temperature (T_K) and the H_2 density (n_{H_2}) of the molecular clumps from the detected emission lines NH_3 (J, K), $J = K = 1, 2$. The masses of molecular clumps are presented and discussed for six unidentified sources in detail in Section 4. For clumps where all data are from HOPS, the NH_3 gas parameters are presented in Purcell et al. (2012). Since our study is particularly interested in those unidentified TeV sources towards star-forming regions, the TeV sources that are towards molecular clumps displaying H_2O maser emission and/or H69α emission are listed in Table 2.

2.1 TeV/molecular clump overlap

Dense molecular clouds were included based on their emission in the NH_3 (1,1) transition. The NH_3 data were smoothed over five velocity channels (~2.0 km s^{-1}), improving the integrated S/N by a factor of ~$\sqrt{5}$. We have classified molecular clouds as significant if their peak emission is > 3σ, where $\sigma \equiv T_{rms}/\sqrt{5}$. Molecular clumps were identified as being towards the TeV emission if the clump centroid position fell within a 3σ radius from the TeV centroid, and adjacent to the TeV emission if the clump centroid position fell between a 3σ and 5σ radius range from the TeV centroid, where σ is the intrinsic rms of the TeV sources quoted in publication (relevant publications are noted in Table 1).

Table 1. TeV sources covered by Mopra 12 mm observations in our study. The 12 mm observations include data from HOPS (Walsh et al. 2011) as well as additional observations undertaken specifically for our study. The HESS TeV source name and centroid position (taken from given references) as well as some alternative names and whether NH_3 (1,1) emission is detected towards, or adjacent to, the source is indicated. Sources highlighted in bold font are discussed in detail in this paper.

HESS name	Alternative name	l	b	NH_3 (1,1) towards	NH_3 (1,1) adjacent	TeV position/size reference
HESS J1023−575	Westerlund 2	284.22	−0.40	–	–	[1]
HESS J1119−614		292.10	−0.49	–	–	[24]
HESS J1303−631		304.24	−0.36	✓	–	[2]
HESS J1418−609	Kookaburra(Rabbit)	313.25	0.15	–	✓	[3]
HESS J1420−607	Kookaburra(PWN)	313.56	0.27	✓	✓	[3]
HESS J1427−608		314.41	−0.14	✓	✓	[4]
HESS J1457−593	G318.2+0.1	318.36	−0.43	–	✓	[5]
HESS J1503−582		319.62	0.29	–	–	[6]
HESS J1614−518		331.52	−0.58	–	✓	[4]
HESS J1616−508		332.39	−0.14	✓	✓	[7]
HESS J1626−490		334.77	0.05	✓	✓	[4]
HESS J1632−478		336.38	0.19	✓	✓	[4]
HESS J1634−472		337.11	0.22	✓	✓	[4]
HESS J1640−465		338.32	−0.02	–	✓	[7]
HESS J1641−463		338.52	0.09	✓	–	[22]
HESS J1646−458	Westerlund 1	339.55	−0.35	✓	✓	[8]
HESS J1702−420		344.30	−0.18	✓	✓	[4]
HESS J1708−410		345.68	−0.47	–	✓	[4]
HESS J1713−397	RX J1713.7−3946	347.34	−0.47	✓	✓	[9]
HESS J1713−381	CTB 37B	348.65	0.38	–	–	[7]
HESS J1714−385	CTB 37A	348.39	0.11	–	–	[10]
HESS J1718−385		348.83	−0.49	–	–	[11]
HESS J1729−345		353.44	−0.13	✓	–	[12]
HESS J1731−347		353.54	−0.67	–	✓	[12]
HESS J1741−302		358.4	0.19	–	–	[13]
HESS J1745−303		358.71	−0.64	✓	✓	[7]
HESS J1800−240A		6.14	−0.63	✓	–	[14]
HESS J1800−240B		5.9	−0.37	✓	–	[14]
HESS J1800−240C		5.71	−0.06	-	✓	[14]
HESS J1801−233	W28	6.66	−0.27	✓	–	[14]
HESS J1804−216		8.4	−0.03	✓	–	[7]
HESS J1808−204		9.96	−0.25	–	–	[23]
HESS J1809−193		11.18	−0.09	✓	✓	[11]
HESS J1813−178		12.81	−0.03	–	✓	[7]
HESS J1818−154	SNR G15.4+0.1	15.41	0.17	✓	–	[15]
HESS J1825−137		17.71	−0.7	–	✓	[7]
HESS J1828−099		21.49	0.38	–	–	[22]
HESS J1831−098		21.85	−0.11	–	–	[16]
HESS J1832−093		22.48	−0.16	✓	–	[17]
HESS J1832−085		23.21	0.29	–	–	[24]
HESS J1834−087		23.24	−0.31	✓	–	[7]
HESS J1837−069		25.18	−0.12	✓	✓	[7]
HESS J1841−055		26.8	−0.2	✓	✓	[4]
HESS J1843−033		29.3	0.51	✓	✓	[18]
HESS J1844−030		29.41	0.09	–	–	[24]
HESS J1846−029		29.7	−0.24	–	–	[19]
HESS J1848−018		31.0	−0.16	✓	–	[20]
HESS J1858+020		35.58	−0.58	–	–	[4]
HESS J1912+101		44.39	−0.07	✓	–	[21]

Notes. [1]Abramowski et al. (2011a); [2]Aharonian et al. (2005); [3]Aharonian et al. (2006b); [4]Aharonian et al. (2008a); [5]Hofverberg (2010); [6]Renaud, Goret & Chaves (2008); [7]Aharonian et al. (2006d); [8]Abramowski et al. (2012); [9]Aharonian et al. (2006a); [10]Aharonian et al. (2008e); [11]Aharonian et al. (2007); [12]Abramowski et al. (2011b); [13]Tibolla et al. (2008); [14]Aharonian et al. (2008b); [15]Hofverberg et al. (2011); [16]Sheidaei, Djannati-Ataï & Gast (2011); [17]HESS Collaboration et al. (2015b); [18]Hoppe (2008); [19]Djannati-Ataï et al. (2008); [20]Chaves et al. (2008); [21]Aharonian et al. (2008d); [22]Abramowski et al. (2014); [23]Rowell et al. (2012); [24]Deil et al. (2015).

The NH_3 (1,1) transition and five further specific molecular transitions were searched for in our study towards the molecular clouds detected with NH_3 (1,1) emission. The transitions were chosen based on their ability to trace star-forming regions at various evolutionary phases and broad-line gas within dense cloud cores. Three inversion–rotation transitions of NH_3, NH_3 (J, K): $J = K = 1$, 2, 3, were chosen in order to estimate gas temperature and density of molecular clumps as well as to identify regions of broad-line
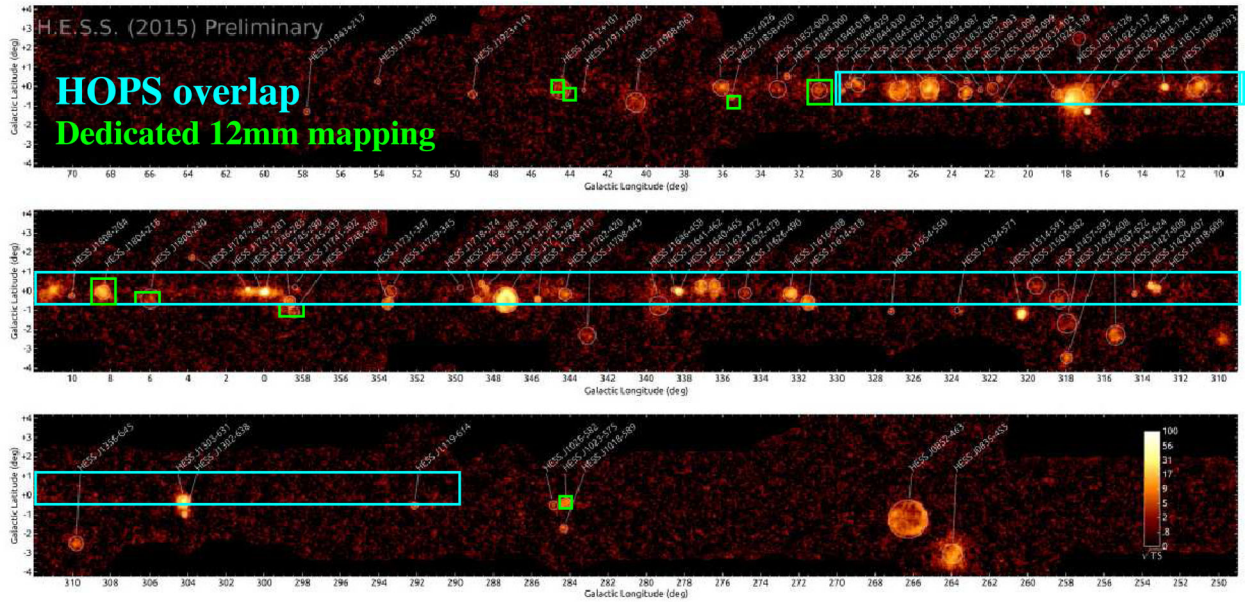
Figure 1. TeV gamma-ray significance image taken from Deil et al. (2015) and overlaid with regions of HOPS 12 mm coverage displayed using cyan boxes and our additional, dedicated 12 mm observations displayed using dashed green boxes.

Table 2. All molecular detections from molecular clumps with NH_3 (1,1) emission towards Galactic TeV sources. This table shows an extract from the full table, which is available in the online appendix. Galactic coordinates of NH_3(1,1) emission, with kinematic distance solutions obtained using the rotation curve of Brand & Blitz (1993), and coincident molecular emission lines.

TeV source	NH_3 (1,1) l	NH_3 (1,1) b	NH_3 (1,1) V_{LSR} (km s^{-1})	kinematic near (kpc)	distance far (kpc)	NH_3 (2,2)	NH_3 (3,3)	HC_3N (3–2)	H_2O (6–5)	H69α
HESS J1729−345	353.3	−0.1	−16.1	3.8	10.3	–	–	–	–	–
HESS J1731−347	353.4	−0.3	−18.7	4.3	9.8	√	√	√	–	–
HESS J1745−303	358.4	−0.5	6.5	–	–	√	–	–	√	–
	358.5	−0.4	−3.7	2.6	10.5	√	√	–	√	–
	358.6	−0.8	2.7	19.5	–	√	–	√	–	–
	358.6	−0.4	−6.7	6.3	–	–	–	–	–	–
	358.8	−0.4	−29.7	–	–	√	√	√	–	–
	358.8	−0.5	−54.0	–	–	√	√	√	–	–
HESS J1800−240C	5.6	−0.1	−27.2	–	–	√	√	√	√	–
	5.8	−0.2	12.0	3.5	10.7	–	–	–	–	–
HESS J1800−240B	5.9	−0.4	7.7	2.3	11.9	√	√	√	√	√
	5.9	−0.3	9.0	2.6	11.5	√	–	√	–	–
HESS J1800−240A	6.6	−0.3	6.0	1.6	12.6	√	√	–	–	–
	6.8	−0.3	20.1	4.7	9.3	√	–	√	√	–
HESS J1804−216	8.1	0.2	18.0	3.7	10.5	√	√	–	–	√
	8.3	0.2	17.1	3.5	10.7	√	–	–	–	–
	8.4	−0.3	36.7	6.7	–	√	√	√	–	–
	8.7	−0.4	36.7	6.4	–	√	√	√	√	–

emission, and unusual gas dynamics. The H_2O maser transition at 12 mm was chosen to identify regions of ongoing star formation that may not show up in IR observations, and the radio recombination line H69α was chosen to identify regions of ionized gas where high-mass stars have been recently formed. The cyanopolyyne transition HC_3N(3–2) was chosen as it, and other cyanopolyyne transitions, is thought to trace early stages of core evolution while NH_3 tends to become more abundant at later stages (Suzuki et al. 1992). The detections of these six molecular transitions are summarized in Table 2.

3 RESULTS OVERVIEW

Out of the 49 TeV sources included in our study, NH_3 (1,1) emission was detected towards or adjacent to 38 of them (see Table 1 for a full list). Between one and nine molecular clumps are seen towards or adjacent to each TeV source. Around half of the molecular clumps detected in NH_3 (1,1) emission display NH_3 (2,2) emission and around one third display NH_3 (3,3) emission. HC_3N (3–2) emission is detected in around one third of molecular clumps, as is the H_2O maser transition, while H69α emission is seen towards less than one fifth of molecular cores. These results are summarized in Table 2.

3.1 NH$_3$ linewidths

The FWHM of the NH$_3$ main line is often used as a measure of the total energy (thermal plus non-thermal) associated with a molecular clump. Broader lines are expected from regions with higher temperatures or additional dynamics (due to turbulence, infall, outflow or tidal flow). The purely Maxwell–Boltzmann thermal linewidth FWHM Δv_{th} expected from a gas at temperature T is given by

$$\Delta v_{\text{th}} = \sqrt{\frac{8\ln(2)kT}{m_{\text{NH}_3}}} \ \text{km s}^{-1}, \tag{1}$$

where k is Boltzmann's constant and m_{NH_3} is the mass of the NH$_3$ molecule. For a temperature of 15 K, as might be expected in typically cold, dense NH$_3$ cores, a thermal linewidth of 0.20 km s^{-1} is obtained (Ho & Townes 1983). The line FWHM of each core was estimated from a Gaussian fit to the main peak of the emission with additional Gaussians to fit each of the four satellite lines, which are generally resolved in the (1,1) transition.

The FWHM for all molecular clumps identified in our study is noticeably wider than that expected from purely thermal broadening, suggesting additional non-thermal or kinetic energy that dominates over broadening from the instrumental response, which in zoom mode at 12 mm provides a velocity resolution of ~0.4 km s^{-1} (Urquhart et al. 2010). Typical linewidth FWHMs observed for NH$_3$ emission in our study are from 1 to 2 km s^{-1}, but in a few cases, very broad linewidths (>10 km s^{-1}) are observed. For NH$_3$ (1,1) emission with very broad linewidths, the satellite lines are blended with the main line that makes fitting the five Gaussian components non-trivial. For these sources, the NH$_3$ (2,2) linewidth (assumed to be unaffected by satellite line blending) was used as an upper limit to the width of the NH$_3$ (1,1) main line, and temperature and density calculated based on this fit. The TeV sources towards which these very broad linewidths are found, HESS J1801$-$233 (the TeV source to the NE of the SNR W28 towards an SNR/molecular cloud interaction region; Nicholas et al. 2011) and HESS J1745$-$303 (Aharonian et al. 2008c), are both thought to be produced hadronically through interaction of accelerated protons and dense gas. The broad linewidths observed towards these sources, together with coincident broad SiO(1–0) emission [which can be seen in Nicholas et al. (2012) for HESS J1801$-$233 and in an upcoming paper for HESS J1745$-$303], indicates the previous passage of a shock through this gas.

3.2 Ortho-to-para NH$_3$ abundance ratios

Para NH$_3$ (1,1) and NH$_3$ (2,2) detections [as well as ortho NH$_3$ (3,3) detections when available] and the LTE methods summarized in Ungerechts et al. (1986) were used to determine the rotational temperatures of all molecular clumps towards TeV sources in the HOPS data set. Towards HESS J1745$-$303 and HESS J1801$-$233 where NH$_3$ (3,3) detections were made, it was noticed when calculating rotational temperatures that the optical depths did not decrease with increasing J (as would be expected) and the NH$_3$ (3,3) brightness temperature $>$ NH$_3$ (1,1) brightness temperature that is shown in Figs 2 and 9 as well as the spectra in Figs 3, 5, 7, 10 and 12. Subsequently, in this work, where NH$_3$ (3,3) brightness temperature $>$ NH$_3$ (1,1) brightness temperature, the NH$_3$ (J, K), $J = K > 2$ emission is not expected to represent the same excitation temperature as the NH$_3$ (1,1) transition and so it is assumed that the NH$_3$ (J, K) $J = K = 3, 4, 5, 6$ emission is optically thin. The molecular clumps towards HESS J1745$-$303 and HESS J1801$-$233 with NH$_3$ (3,3) brightness temperature $>$ NH$_3$ (1,1) brightness temperature
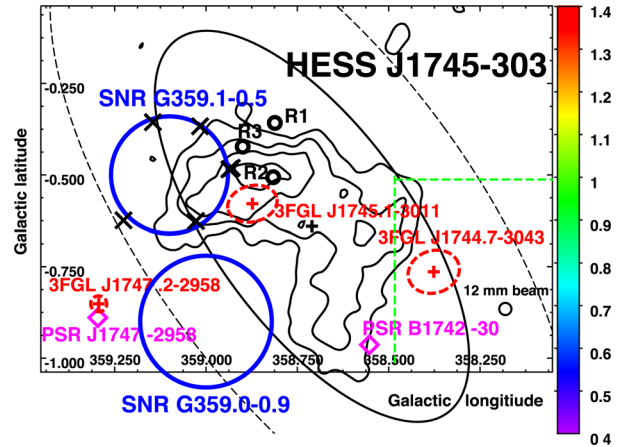

Figure 2. An image of NH$_3$ (3,3) peak pixel-to-NH$_3$ (1,1) peak pixel emission towards TeV source HESS J1745$-$303. The image has been produced to only show the ratio in regions of significant NH$_3$ (3,3) emission, although some scanning artefacts from noisy pixels are still visible towards the Galactic east and south edges of the mapping region. This image is overlaid with contours of TeV emission (black) and the regions towards which the deep pointing spectra were taken (small black circles). SNRs are indicated as large, solid blue circles, 1720 MHz OH masers are indicated with black $\times$s and pulsars are indicated as magenta diamonds.
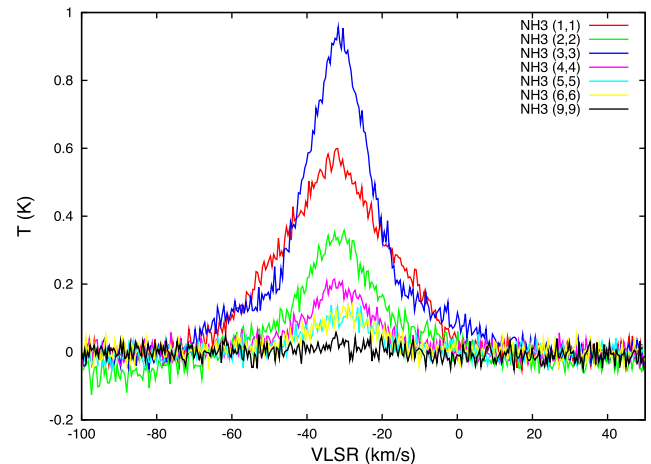

Figure 3. NH$_3$ (J, K) $J = K = 1, 2, \ldots, 6$ spectra from the region marked as region 1 towards HESS J1745$-$303 in Fig. 2. The peak brightness temperature of the NH$_3$ (3,3) emission is greater than that of the other transitions.

were found to have extended emission in all four of the metastable ammonia transitions considered in the HOPS observations [NH$_3$ (J, K), $J = K = 1, 2, 3, 6$]. The molecular clouds towards both HESS J1745$-$303 and HESS J1801$-$233 exist close to SNRs that are interacting with molecular clouds, evident by 1720 MHz OH masers. In addition, 7 mm observations of the regions displaying NH$_3$ (3,3)-to-NH$_3$ (1,1) brightness temperature ratios > 1 revealed extended SiO (1–0) emission that matches the morphology of the NH$_3$ emission.

Upper-state column densities for each transition were calculated using the LTE analysis summarized by Ungerechts et al. (1986). These values were divided by the total degeneracy (angular momentum degeneracy, $g_u = 2J + 1$ as well as spin and K degeneracy) and used to plot rotation diagrams. Rotation diagrams shown in Figs 4, 6, 8, 11 and 13 include upper-state column densities of each observed transition towards each region of extended NH$_3$ emission
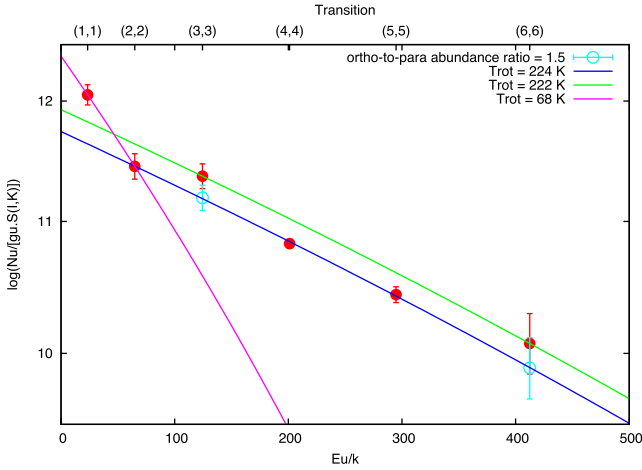
Figure 4. Rotation diagram for region 1 of HESS J1745−303 (shown in Fig. 2) where N_u, g_u and E_u are the column density, the statistical weight and the energy for the upper levels of the transitions NH$_3$ (J, K) $J = K = 1$, 2, ..., 6. Rotational temperatures, $T_{\rm rot} = 1/$slope, have been determined for three groups of transitions, and it can be seen, since the slopes are very similar, that the rotational temperature is similar for the ortho NH$_3$ (3,3) and (6,6) transitions and the para NH$_3$ (4,4) and (5,5) for which the rotational temperature given here was fitted along with the OPR adjusted ortho column densities (shown as open cyan circles). Here an OPR of 2.0 was estimated. The best-fitting OPR is 1.5 ± 0.5.
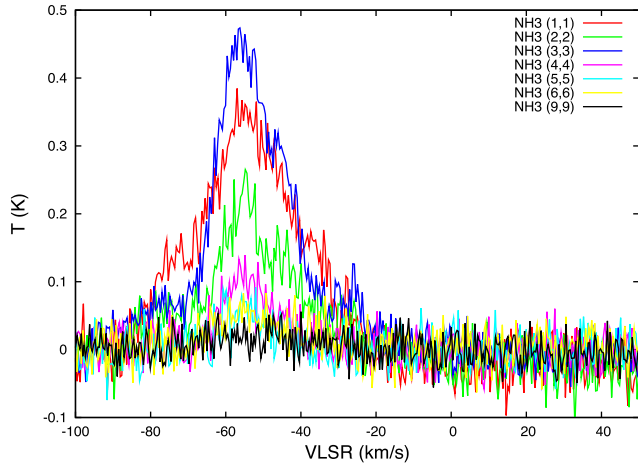
Figure 5. NH$_3$ (J, K) $J = K = 1, 2, \ldots, 6$ spectra from the region marked as region 2 towards HESS J1745−303 in Fig. 2. The peak brightness temperature of the NH$_3$ (3,3) emission is greater than that of the other transitions.

where NH$_3$ (3,3) brightness temperature $\geq$ NH$_3$ (1,1) brightness temperature. The rotation temperature of para NH$_3$ was estimated separately for the NH$_3$ (J, K) $J = K = 1$, 2 transitions and the NH$_3$ (J, K) $J = K = 4$, 5 transitions. The rotational temperature of ortho NH$_3$ was estimated using the NH$_3$ (J, K) $J = K = 3$, 6 transitions, and it is assumed that $T_{36} = T_{45}$.

ON/OFF deep pointing observations were taken at three positions towards HESS J1745−303, and two positions towards HESS J1801−233. These regions indicated in Fig. 2, which were chosen due to their high NH$_3$ (3,3)-to-(1,1) brightness temperature ratios, and Fig. 9, which were chosen due to their positions immediately post-shock and pre-shock where the shock position is traced by 1720 MHz OH masers. The method of Umemoto et al. (1999) was used to estimate the ortho-to-para NH$_3$ abundance
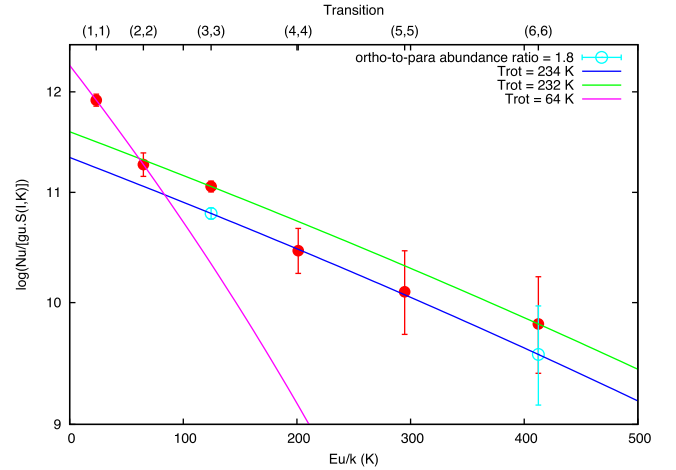
Figure 6. As in Fig. 4, for region 2 of HESS J1745−303 (shown in Fig. 2). For this region, an OPR of 2.0 was estimated. The best-fitting OPR is 1.8 ± 0.6, indicating an OPR enhancement. This region lies towards the centroid of TeV gamma-ray emission.
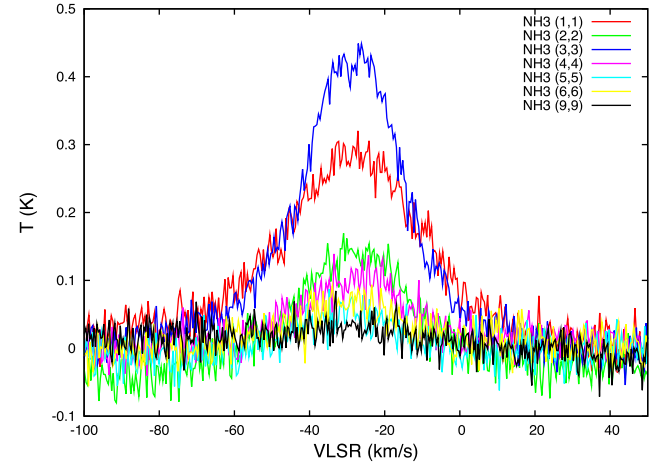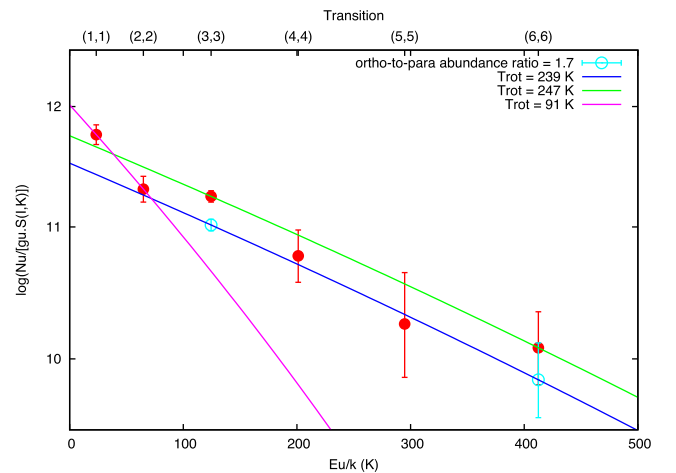

Figure 7. NH$_3$ (J, K) $J = K = 1, 2, \ldots, 6$ spectra from the region marked as region 3 towards HESS J1745−303 in Fig. 2. The brightness temperature of the NH$_3$ (3,3) emission is greater than that of the other transitions.

Figure 8. As in Fig. 4, for region 3 of HESS J1745−303 (shown in Fig. 2). For this region, an OPR of 1.5 was estimated. The best-fitting OPR is $1.7^{+0.3}_{-0.4}$.
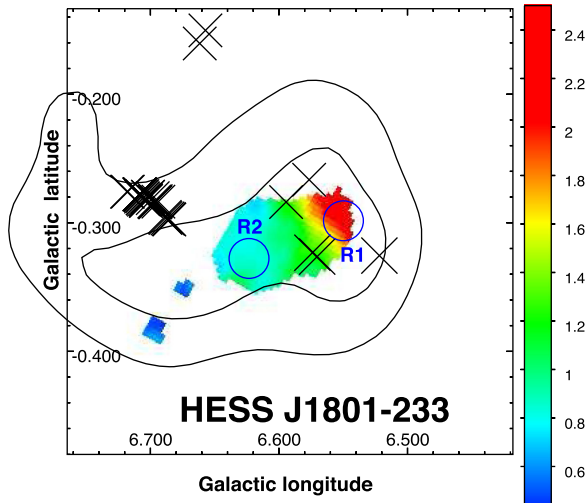
Figure 9. An image of NH_3 (3,3) peak pixel-to-NH_3 (1,1) peak pixel emission towards TeV source HESS J1801−233. This image is overlaid with contours of TeV emission (black) and the regions towards which the deep pointing spectra were taken (blue circles). 1720 MHz OH masers are indicated with black ×s.
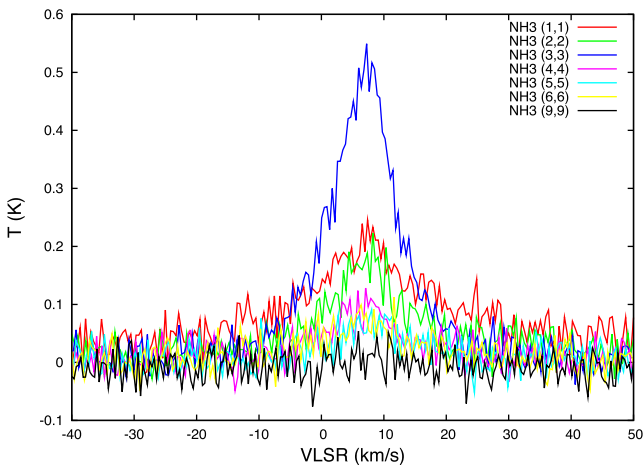

Figure 10. NH_3 (J, K) $J = K = 1, 2, \ldots, 6$ spectra from the region marked as region 1, towards HESS J1801−233, in Fig. 9. This region is post-shock as the 1720 MHz OH masers effectively mark the current position immediately post-shock, and the SNR is expanding with the shock moving towards region 2. These spectral lines all display broad (>6 km s^{-1}) linewidths, and this region also displays extended SiO(1–0) emission. The brightness temperature of the NH_3 (3,3) emission is greater than that of the other transitions.

ratio. Figs 4, 6, 8, 11 and 13 display a straight line fit to the derived NH_3 (4,4) and (5,5) column densities, where 1/slope = T_{rot}. This rotational temperature was compared to the T_{rot} fit for the ortho NH_3 (3,3) and (6,6), and in many cases the lines fitting each pair of column densities are almost parallel (indicating an equivalent T_{rot}). Ortho-to-para NH_3 abundance ratios were estimated and used to produce reduced ortho NH_3 (3,3) and (6,6) column densities (ROCDs) according to

$$ROCD = N_{ortho}/OPR_{est}, \qquad (2)$$

where N_{ortho} is the upper-state ortho NH_3 column density for each transition and OPR_{est} is the estimated NH_3 ortho-to-para abundance ratio. These 'reduced' ortho NH_3 column densities were then optimised with least-squares fitting with a straight line fit to all NH_3
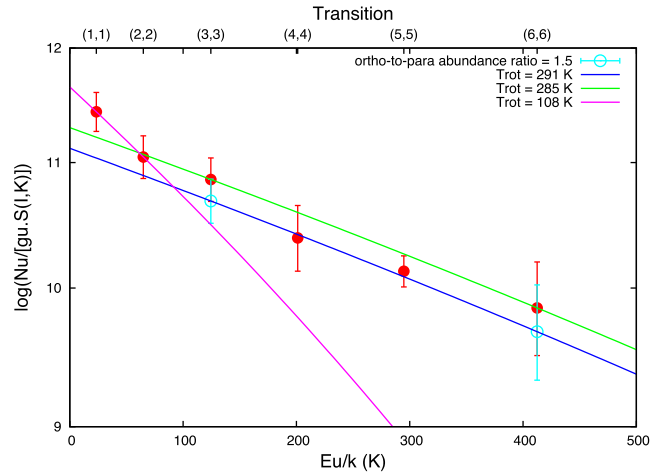

Figure 11. As in Fig. 4, for region 1 of HESS J1801−233 (shown in Fig. 9). For this region, an OPR of 1.5 was estimated. The best-fitting OPR is 1.5 ± 0.5. This region is the post-shocked region.
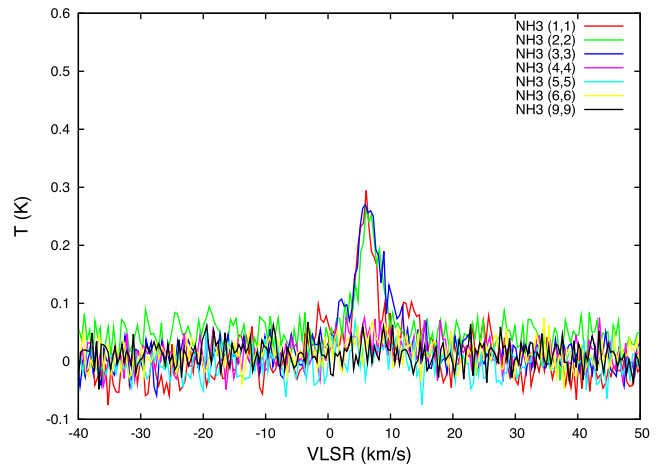

Figure 12. NH_3 (J, K) $J = K = 1, 2, \ldots, 6$ spectra from the region marked as region 2, towards HESS J1801−233, in Fig. 9. This region is pre-shock as the 1720 MHz OH masers effectively mark the current position immediately post-shock, and the SNR is expanding with the shock moving towards region 2. The brightness temperature of the NH_3 (3,3) emission is slightly less than that of the NH_3 (1,1) emission and slightly greater than that of the NH_3 (2,2) emission.

(J, K) $J = K = 3, 4, 5, 6$ column densities. The OPR that gives the best fit is given in Table 3.

It can be seen in Table 3 that for all three regions investigated towards HESS J1745−303, an OPR ≥ 1 is indicated (see Table 3). We believe that an OPR ≥ 1 indicates the previous passage of a shock through a gas cloud (see Section 1). The regions observed towards HESS J1745−303 with an OPR ≥ 1 lie outside the boundary of the SNRs in the region indicating that another shock is responsible for the enhancement of ortho NH_3 over para NH_3. Several radio continuum point sources, centred on a molecular CO(1–0) ring in the region, may be remnants of an OB association responsible for a superbubble (Uchida et al. 1992).

ON–OFF deep pointing observations were taken at two positions towards HESS J1801−233. These regions are indicated in Fig. 9 and were chosen due to their positions immediately post-shock and pre-shock where the shock position is traced by 1720 MHz OH masers.
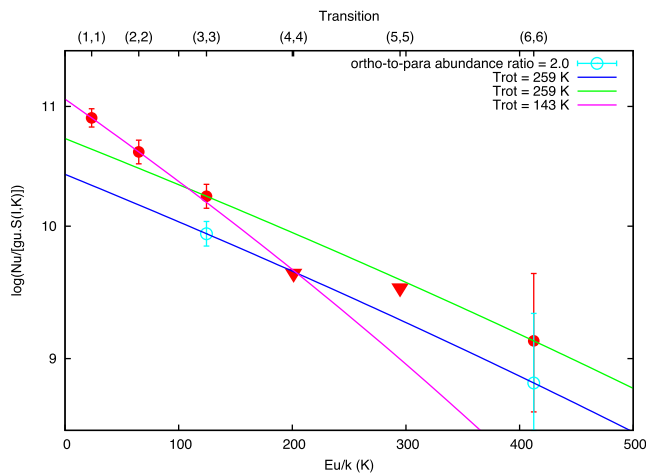
Figure 13. As in Fig. 4, for region 2 of HESS J1801−233 (shown in Fig. 9). For this region, an OPR of 1.5 was estimated. A lower limit OPR has been found (due to upper limits of NH₃ (4,4) and (5,5) emission). This method indicates an OPR of >2.0. As can be seen in this image however, the NH₃ (3,3) and upper limit NH₃ (4,4) column densities, with an OPR of 1.0, lie on the rotational temperature fit to the NH₃ (1,1) and (2,2) emission (magenta line) indicating that the gas traced by these transitions may have an OPR of 1.0 and have a rotational temperature of that given by the NH₃ (1,1) and (2,2) transitions. The NH₃ (5,5) and (6,6) emission would then be tracing higher temperature gas, and the derived OPR would not reflect the conditions of this gas. This region is the pre-shocked region of molecular gas associated with HESS J1801−233.

For HESS J1801−233, the method used here cannot determine whether the OPR is enhanced in the regions indicated in Fig. 9. Region 1 is immediately post-shock and region 2 is immediately pre-shock where the shock position is traced by 1720 MHz OH masers. The best fit indicates that the OPR is enhanced in both regions that is consistent with a previous study (Maxted et al. 2016) using NH₃ (J, K), J = K = 1, 2, 3, 4, 6 to estimate the OPR in region 1. For region 2 (indicated in Fig. 9), the rotational temperature for NH₃ (1,1) and (2,2) fits to the column densities of transitions up to the NH₃ (4,4) upper limit (as can be seen in Fig. 13), which may indicate that the higher J NH₃ (5,5) and (6,6) transitions are tracing a higher temperature component of the gas. If this were the case, the lower limit OPR for this region would not reflect the conditions of the gas. An enhanced OPR would not be expected in this region. In region 1 (indicated in Fig. 9), the post-shocked region,

the determined OPR is consistent with 1, within errors; however, an enhanced OPR could be expected in this region.

3.3 TeV emission from PWNe

Pulsar wind nebulae or old relic PWNe are thought to be responsible for the TeV emission from many of the unidentified Galactic gamma-ray sources (Chang, Konopelko & Cui 2008; Mattana et al. 2009). The population of likely TeV PWNe is thought to include 27 sources (de Oña-Wilhelmi et al. 2013), although many of these sources do not have associated, observed pulsars. Gallant et al. (2008) have identified seven TeV sources as confirmed PWNe. We have added HESS J1303−631 to this list as it has been since confirmed as a PWN (H.E.S.S. Collaboration et al. 2012), and meets the same requirements for confirmed PWNe proposed by Gallant et al. (2008).

In order to assess whether TeV sources in our study meet energetics constraints provided by confirmed PWNe, we have assumed that the TeV emission is at the same distance as the dense molecular gas traced by NH₃ (1,1) emission and scaled the TeV luminosity of each source accordingly. We then calculated the range of spin-down powers a pulsar producing this emission could have if the TeV emission was between 0.01 per cent and 7 per cent of the pulsar spin-down power [as is the case for the population of seven confirmed PWN in Gallant et al. (2008)]. In Fig. 14, the range of TeV luminosities for all TeV sources included in this study, along with the range of spin-down powers these luminosities would translate to, with minimum and maximum TeV efficiencies of 0.001 per cent and 7 per cent, respectively. It can be seen that, even with minimum TeV efficiency, the range of inferred spin-down powers is between 10^{34} and 10^{39} erg s⁻¹, a range consistent with the population of pulsars likely to have an association with TeV emission identified by de Oña-Wilhelmi et al. (2013). Therefore, all of the TeV sources included in this study of dense gas detected by NH₃ (1,1) adjacent to TeV emission meet energetics requirements to be Galactic PWNe.

In addition, we believe that the range of inferred spin-down powers in Fig. 14 indicates that there could be a population of older TeV emitting PWNe, in the population of TeV sources included in this study, with a higher TeV efficiency (i.e. close to the maximum current TeV efficiency seen of 7 per cent, or even greater), which do not yet have associated, detected pulsars considered likely to have an association with TeV emission identified by de Oña-Wilhelmi et al. (2013). This population of TeV emitting PWNe is likely to become
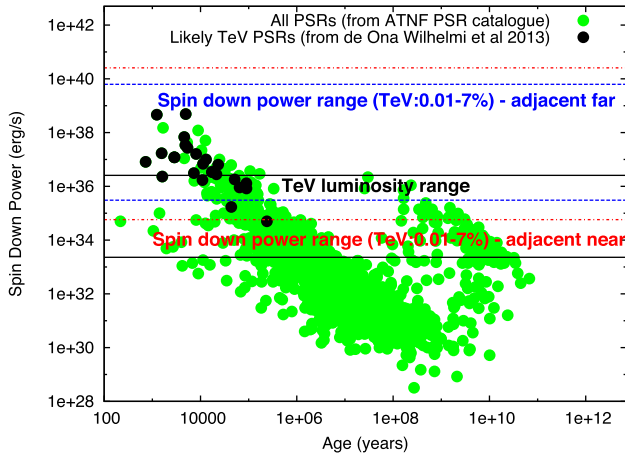
Table 3. The T_{rot} given for NH₃ (3,3)-to-(6,6) (reduced ortho) = 1/slope of the line fit to the column densities for regions defined in Figs 2 and 9 (adjusted according to the estimated NH₃ OPR) of the transitions for NH₃ (J, K) J = K = 3, 4, 5, 6. The OPR given is that with the best fit to the NH₃ (J, K) J = K = 3, 4, 5, 6 column densities. The * indicates a region where the apparent OPR fitted appears to be due to an incorrect division of transitions into temperature components rather than an enhanced OPR. Further details are outlined in the caption of Fig. 13.

TeV source and region	T_{rot} para (1,1),(2,2) (K)	T_{rot} ortho (3,3),(6,6) (K)	T_{rot} para (4,4),(5,5) (K)	T_{rot} (3,3)-(6,6) (reduced ortho) (K)	OPR best fit
HESS J1745−303					
region 1	68	222	239	224	1.5 ± 0.3
region 2	64	256	232	234	1.8 ± 0.6
region 3	91	247	181	239	$1.7^{+0.3}_{-0.4}$
HESS J1801−233					
region 1	108	285	360	291	1.5 ± 0.5
region 2	143	259	–	–	>2.0*

Figure 14. Spin-down power versus age for pulsars from the ATNF Pulsar Catalogue (Manchester et al. 2005) plotted with green dots. The population of pulsars deemed as likely TeV PWNe by de Oña-Wilhelmi et al. (2013) have been overplotted with black dots. It can be seen that the minimum spin-down power for those pulsars likely associated with TeV emission is $\sim 10^{34}$ erg s^{-1}. The TeV luminosity range (scaled according to molecular clump distance) is indicated by black, solid lines. The range of spin-down powers for minimum apparent TeV efficiencies of 0.001 per cent and maximum apparent TeV efficiencies of 7 per cent for adjacent clumps' near and far distances are indicated by blue dashed and red dot–dashed lines, respectively.

more apparent with the increasing sensitivity of TeV gamma-ray observations.

This method has not allowed for discrimination based on energetics requirements for those sources that are currently unidentified, which may be PWNe. Fig. 14 demonstrates this as TeV luminosities derived for all molecular cores detected in our study fall within the expected range for TeV emitting PWNe. This study is useful for more detailed studies for individual TeV sources that compare the morphology of dense gas with the TeV emission (e.g. Voisin et al. 2016). In the case of PWNe, which are produced leptonically through IC emission, the TeV emission often exhibits asymmetric morphology, and is expected to anti-correlate with molecular gas. This asymmetry can be explained by an inhomogeneous distribution of interstellar gas around pulsars that strongly influences their development (e.g. Blondin et al. 2001). This study can be used to search for dense gas anti-correlated with asymmetric morphology of TeV emission to identify relic PWNe. In addition, these relic PWNe would be less likely to display 2–10 keV X-ray emission than the younger PWNe, in accordance with the ratio of gamma-ray to X-ray flux identified by Mattana et al. (2009) to increase with PWN age.

4 DISCUSSION OF SIX PROMINENT UNIDENTIFIED TEV SOURCES

Six TeV sources that have not been unambiguously connected to any counterpart at other wavelengths are discussed in detail here. These sources were chosen for their coincidence with star-forming regions as evident by IR emission, H_2O masers and/or H69α emission or, as for HESS J1745−303, an anomalous NH_3 ortho-to-para brightness temperature ratio. Images of the peak pixel brightness temperature between velocities of −200 and 200 km s^{-1} of various molecular transitions along with spectra towards selected molecular gas clumps and IR features are displayed in Figs 15–26. A discus-

sion of notable gas and IR features is included in the following section. The molecular transition gas maps seen in Figs 15–25 have been chosen based on significant emission (defined as $> 3\sigma$, where $\sigma \equiv T_{rms}/\sqrt{5}$) seen towards or adjacent to the TeV emission. Maps of the other transitions searched for are not shown.

For the sources for which the TeV could possibly originate from CR protons, a simple calculation of diffusion time has been used to help assess the plausibility of the TeV emission coming from interactions between CRs from a nearby accelerator and dense gas catalogued in this survey.

To calculate the distance d travelled by CR protons in a given time, t, we have used

$$d = \sqrt{2D(E_p, B)t}, \tag{3}$$

where $D(E_p, B)$ is the diffusion coefficient dependent on maximum proton energy, E_p, and magnetic field B according to

$$D(E_p, B) = \chi D_0 \left(\frac{E_p/\text{GeV}}{B/3\,\mu\text{G}} \right)^{0.5} \text{cm}^2\,\text{s}^{-1} \tag{4}$$

from Gabici, Aharonian & Blasi (2007). D_0 is the average Galactic diffusion coefficient (Berezinskii et al. 1990), χ is the diffusion suppression coefficient (assumed to be <1 inside molecular cores; 1 outside; Berezinskii et al. 1990; Gabici et al. 2007). The magnetic field strength as a function of density n_{H_2} cm^{-3} using

$$B(n_{H_2}) \sim 10 \left(\frac{n_{H_2}}{300\,\mu\text{G}} \right)^{0.65} \mu\text{G} \tag{5}$$

was taken from Crutcher (1999) based on their Zeeman splitting measurements in molecular clouds.

4.1 HESS J1745−303

HESS J1745−303 in Fig. 15 is a source where NH_3 (1,1) emission is coincident with the TeV peak. Of particular interest here is the broad-line emission of all thermal molecular line transitions towards the TeV centroid. HESS J1745−303 partially overlaps both the molecular cloud and the SNR G359.1 − 0.5. The SNR G359.1 − 0.5 interacts with a molecular cloud as evident by a cluster of 1720 MHz OH masers towards the SNR rim. This SNR has been attributed to producing this broad-line emission; however, the broad-line emission has a kinematic velocity that differs from that of the masers by around 50 km s^{-1} and the broad emission line region lies outside the boundary of the SNR observed in radio continuum (see Fig. 15 where the SNR boundary is indicated). Broad-line molecular gas is only observed towards one region of the gamma-ray emission, defined as region A by Aharonian et al. (2008c, and indicated in Fig. 15), which includes the highest TeV gamma-ray significance region, the 7σ contour. The molecular line emission detected in our study, within the 7σ significance contour, includes this broad emission line cloud (FWHM > 10 km s^{-1}), the spectra of which are displayed in the LHS of Fig. 15. In addition to broad emission lines, NH_3 (3,3) emission is observed to have a higher peak brightness temperature than NH_3 (2,2) and (1,1). As discussed in Section 3.2, this molecular cloud has an enhanced ortho-to-para NH_3 abundance ratio that we believe is due to the previous passage of a shock through the cloud. The nature of the shock is not clear as this gas is outside the boundary of the observed SNRs in the region. Non-thermal broadening (i.e. from turbulence) of these spectral lines dominates over the thermal broadening (<4 km s^{-1}), which further supports that a shock has passed through this molecular cloud. This will be discussed in more detail in a future study (de Wilt & Rowell, in preparation).
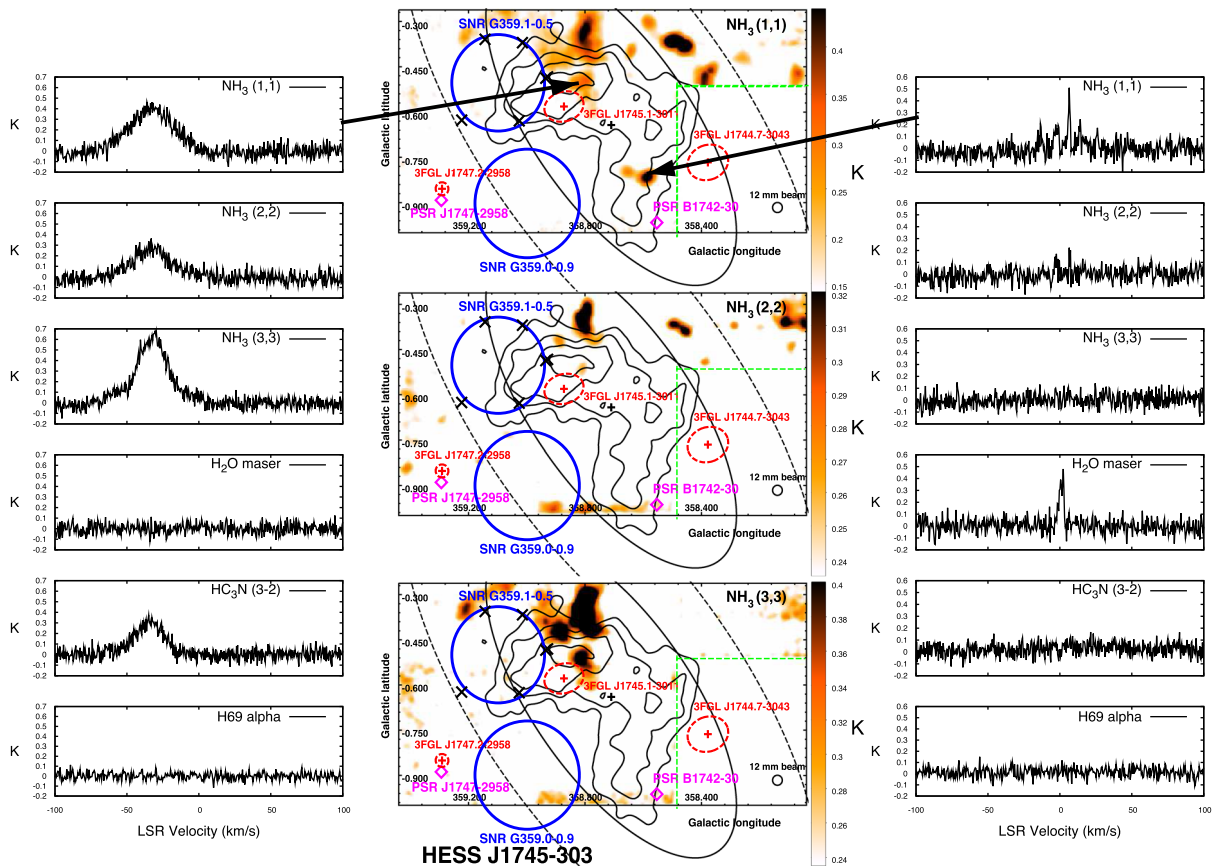
Figure 15. 12 mm peak pixel maps of molecular line emission towards the TeV source HESS J1745−303. TeV significance contours (4σ–7σ; Aharonian et al. 2008c) are shown in black. Images of the peak pixel along the line of sight between LSR velocities −200 and 200 km s^{-1} of NH$_3$ (J, K), ($J = K = 1$, 2, 3) are seen. Broad-line emission is displayed in the spectra of all thermal lines seen towards the 7σ TeV significance contour; however, no H$_2$O masers or H69α emission is detected in our study. Spectra from a dense cloud core towards the SW component of TeV emission are seen (on the RHS here) offset in velocity from the broad emission by $\sim$55 km s^{-1}. The size of the region each of the spectra displayed in this image and Figs 17, 19, 21, 23 and 25 is taken from is given by one 12 mm beam size (displayed in each image).

There are several other potential sources of CR hadrons and/or electrons in the region that include two energetic pulsars, an additional SNR, G359.0−0.9 (all of which are indicated in Fig. 15), and a further radio continuum feature seen in archival data taken as part of the Molonglo Galactic Plane Surveys (Green 1999), which could potentially be another SNR (see de Wilt et al., in preparation).

Previous studies have discussed the lack of molecular cloud emission towards the west and south-west components of TeV emission in HESS J1745−303 (e.g. Aharonian et al. 2008c; Hayakawa et al. 2012). Our study confirms a lack of broad molecular line emission towards these components of TeV emission, and therefore suggests that there are no Galactic ridge molecular cloud counterparts to the west and south-west components of the TeV source. We have identified dense molecular gas through NH$_3$ transitions that are found towards region B [as defined by Aharonian et al. (2008c) and seen in Fig. 15], which may be associated with the TeV emission. The NH$_3$ emission from these dense gas cloud cores exhibits narrow linewidths ($<$4 km s^{-1}) that suggests that the emission is foreground or background to the Galactic Centre (GC). Purcell et al. (2012) state that the sensitivity of the HOPS observations means that it is unlikely that any emission seen is background to the GC, which makes it likely that these clouds are foreground to the GC. The association between this newly detected gas and the TeV emission is being investigated further, and the results will be presented in a future paper. The narrow-line NH$_3$ (1,1) emission extent and spectrum can be seen in Fig. 15.

Fig. 16 shows that no active star formation is seen overlapping the TeV centroid in either the *Spitzer* IR bands nor in the molecular tracers used in our study. A similar situation is seen towards HESS J1801−233, the TeV peak towards the interacting SNR W28 (Nicholas et al. 2011). The lack of IR emission here supports the interpretation of the broad-line emission not being associated with heating due to star formation processes, but perhaps due to additional energetics such as kinetic energy provided by a shock that has passed through the gas cloud. As the gas lies outside the boundary of the SNR G359.1−0.5 as seen in radio continuum, we propose that there has been another shock that has passed through the cloud, producing the post-shocked gas characteristics of broad-line emission, an ortho-to-para brightness temperature ratio $>$ 1 as well as extended SiO (1–0) emission.

4.2 HESS J1640−465

Fig. 17 displays NH$_3$ (1,1) emission towards the edges of the TeV gamma-ray source HESS J1640−465. The gamma-ray emission is seen towards the SNR G338.3−0.0 and a giant H II region G338.4+0.1, both detected in radio continuum at 843 MHz (Whiteoak & Green 1996). The faint *ASCA* X-ray source AX

Table 4. All molecular detections from molecular clumps with NH₃ (1,1) emission towards Galactic TeV sources. This table shows an extract from the full table, which is available from the online appendix. For individual sources such as HESS J1745−303, the large spread of distances between different molecular clouds may be due to the clouds being located at different distances along the line of sight, or perhaps due to intrinsic movement of the molecular clouds. HESS J1745−303 is located close to the CMZ, and so the Galactic rotation curve used here does not include solutions for the distances to several molecular clouds observed. For HESS J1745−303, we believe that the clouds are separated into several distinct distance groups. These distance ambiguities will be investigated further in an upcoming paper (de Wilt & Rowell, in preparation).

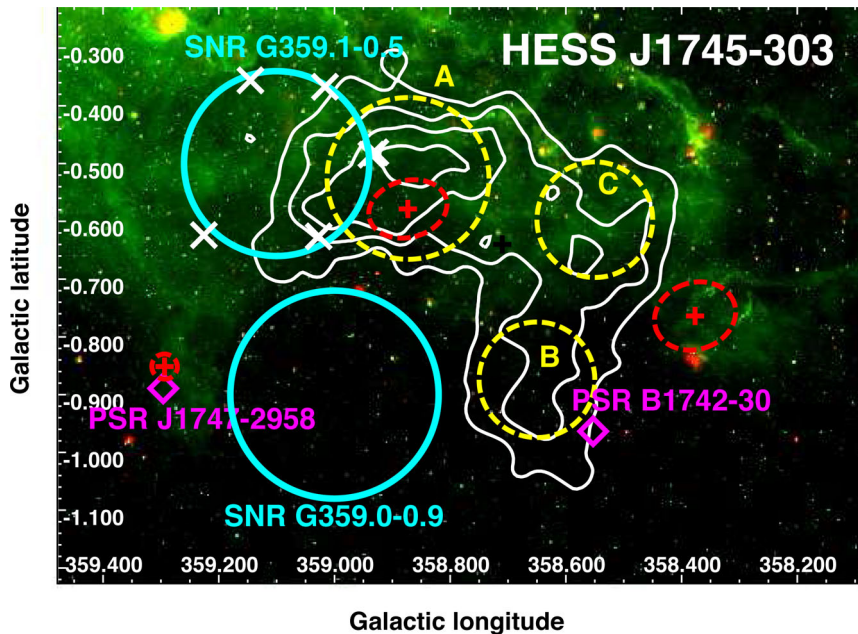| TeV source	NH_3 (1,1) l	NH_3 (1,1) b	NH_3 (1,1) V_{LSR} (km s^{-1})	kinematic near (kpc)	distance far (kpc)	H_2 mass (near) $M_\odot$	N_{NH_3} $\times 10^{13}$ (cm^{-2})	H_2 density (cm^{-3})
HESS J1626−490	334.71	0.04	−86.46	5.5	8.6	0.2	7.7	1.3×10^3
HESS J1640−465	338.09	0.01	−40.00	3.3	11.2	1153	8.4	5.8×10^2
	338.33	0.14	−36.59	3.1	11.4	100	1.3	1.2×10^2
	338.47	0.04	−37.01	3.2	11.3	975	5.2	3.1×10^2
HESS J1729−345	353.28	−0.06	−16.09	3.9	10.2	–	–	–
HESS J1745−303	358.37	−0.46	6.50	–	–	353	1.2	0.6×10^2
	358.46	−0.38	−3.73	3.3	9.3	186	2.4	2.2×10^2
	358.59	−0.81	2.66	19.4	–	–		
	358.64	−0.40	−6.71	6.3	–	0.1	0.4	6.7×10^2
	358.80	−0.36	−29.73	–	–	23 827	11.1	2.0×10^2
	358.81	−0.51	−54.02	–	–	–		
HESS J1804−216	8.14	0.22	17.96	3.7	10.5	517	3.0	1.8×10^2
	8.25	0.17	17.10	3.5	10.7	212	1.4	1.0×10^2
	8.40	−0.28	36.71	6.7	–	7669	3.4	0.6×10^2
	8.68	−0.40	36.71	6.4	–	8091	4.8	1.0×10^2
HESS J1848−018	30.72	−0.07	92.16	5.2	9.2	1942	6.3	2.9×10^2
	30.78	−0.08	94.30	5.1	9.1	1.2	4.8	8.1×10^3
	30.81	−0.04	93.87	5.1	9.1	1909	5.9	2.6×10^2
	30.98	−0.14	77.25	4.4	10.0	–	–	–

Figure 16. *Spitzer* GLIMPSE/MIPSGAL three-colour (RGB = 24/8/4.5 µm M Jy sr^{-1}) image of the region towards HESS J1745−303 (the TeV emission is indicated by white contours). Several 'rings' can be seen in the green, 8 µm emission; however, there is no indication of star formation in these IR bands towards the TeV emission.

J1640.7−4632 (see Sugizaki et al. 2001) is coincident with HESS J1640−465, as is the *Fermi*-Large Area Telescope (LAT) source 3FGL J1640.4−4634. A separate TeV source named HESS J1641−463, with a harder spectral index, to the edge of this TeV source is seen (see Lemoine-Goumard et al. 2014) towards the SNR G338.5+00.1. The molecular line emission seen in HOPS data shows broad (∼5 km s^{-1}) NH₃ emission in the (1,1)-to-(3,3) inversion transitions, indicative of shocked/excited gas towards the giant H II region G338.4+0.1, located between the two TeV sources. Several H₂O masers (Walsh et al. 2011) are seen towards and surrounding this TeV source (seen in Fig. 17), indicating the ongoing star formation in the region. All of the detected molecular line
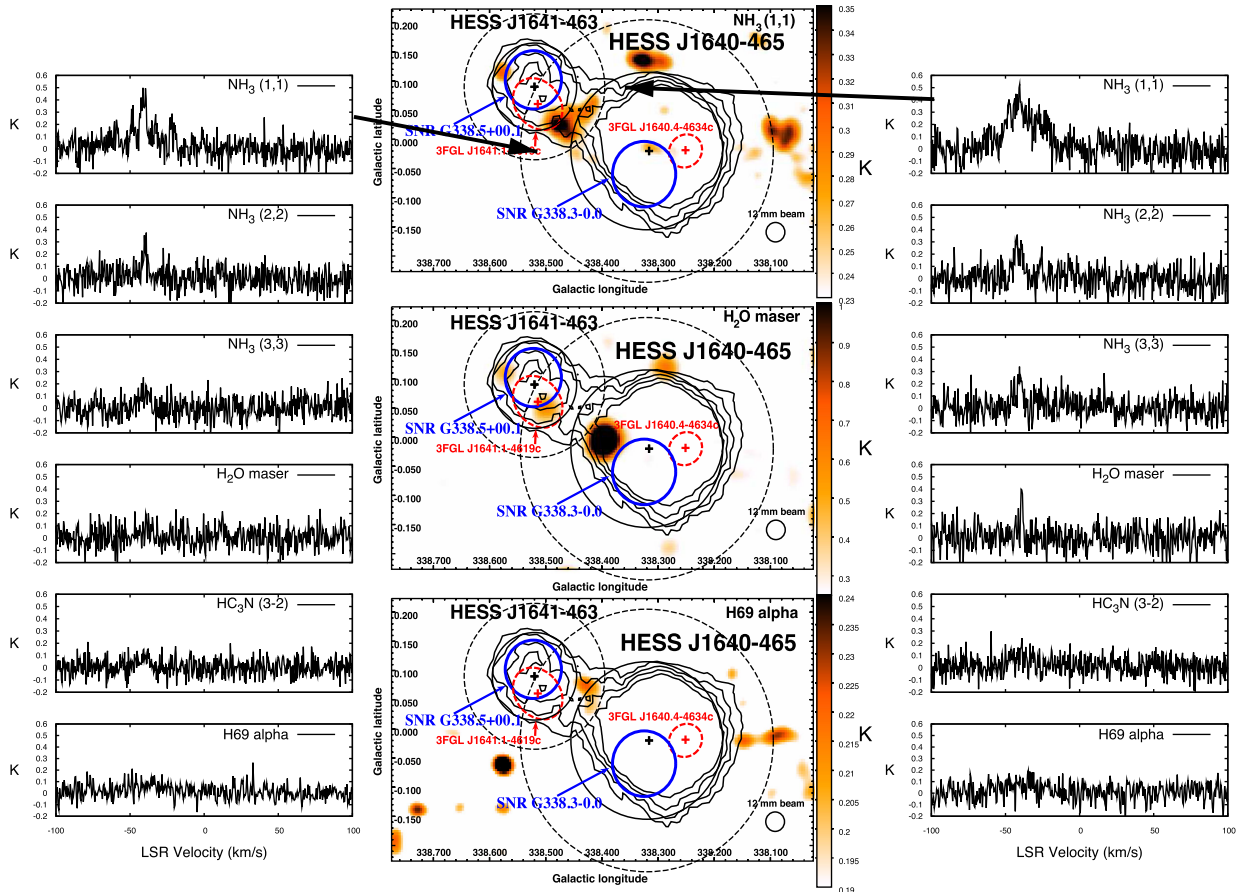
Figure 17. 12 mm peak pixel maps of molecular line emission towards the TeV source HESS J1640−465 (which is indicated by solid, black contours) and the newly discovered HESS J1641−463 (the centroid of which is indicated by a +, and the intrinsic size indicated by a dashed circle). Three gas clumps are seen traced by NH$_3$ (1,1) emission, all adjacent to the TeV emission. Two of these clumps (for which the spectra are shown above) display H$_2$O maser emission and H69α emission indicating both ongoing star formation and ionized gas.
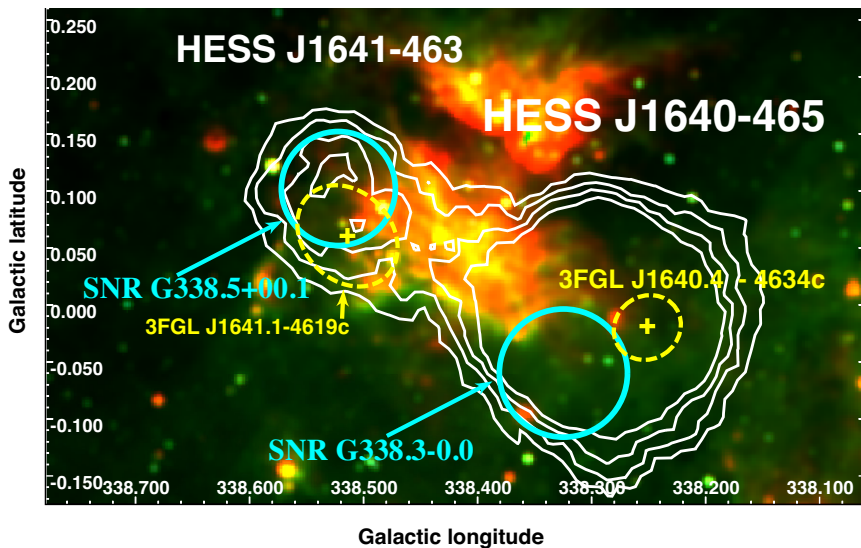
Figure 18. *Spitzer* GLIMPSE/MIPSGAL three-colour (RGB = 24/8/4.5 μm M Jy sr^{-1}) image of the region towards HESS J1640−465 and HESS J1641−463. Two giant H II complexes are seen as prominent features of this image. G338.4+0.1 lies between the two TeV sources. These H II complexes are both traced by H69α in our study (seen in Fig. 17).

transitions have a far kinematic distance matching that of both of the SNRs in the region (~11 kpc; Kothes & Dougherty 2007).

The pulsar PSR J1640−4631 has been recently discovered by Gotthelf et al. (2014), using the *Nuclear Spectroscopic Telescope Array*, towards HESS J1640−465 with a spin-down luminosity of 4.4×10^{36} erg s^{-1}. The pulsed X-ray emission and the TeV centroid of HESS J1640−465 occur at the centre of the SNR G338.3−0.1. This, together with the morphology of the molecular material detected in our study (which surrounds the TeV emission), may favour a PWN model for the TeV emission. Rescaling the TeV flux (>1 TeV) to the distance of the SNRs and NH$_3$ emission gives a gamma-ray luminosity of 2.4×10^{34} erg s^{-1}. Assuming that PSR J1640−4631 is linked to SNR G338.2−0.0, and so is at a distance of 11 kpc, and is powering the PWN HESS J1640−465, the apparent efficiency of PSR J1640−4631 would be ~0.05 per cent, within the range of confirmed TeV PWNe, 0.01 to 7 per cent (Gallant et al. 2008).

3FGL J1640.4−4634, also catalogued as 1FGL J1640.8−4634, the *Fermi*-LAT GeV source coincident with HESS J1640−465, has a spectrum (from five years of *Fermi*-LAT data) that joins smoothly to the TeV spectrum (Lemoine-Goumard et al. 2014). This smooth spectrum from GeV to TeV favours a hadronic origin to the TeV gamma-rays, and has been reproduced by a hadronic model of HESS J1640−465 (Lemoine-Goumard et al. 2014); however, the spectrum can also be reproduced by fine tuning to a leptonic, PWN model (see Gotthelf et al. 2014), and so this possibility cannot be ruled out.

Adjacent to HESS J1640−465 is the TeV source HESS J1641−463 (Abramowski et al. 2014). This source has a harder spectral index than HESS J1640−465 and several possible counterparts including SNR G338.5+0.1; several X-ray sources (which may point towards a PWN scenario) have been identified (Abramowski et al. 2014). HESS J1641−463 could also be a TeV binary system, although no variability in TeV gamma-rays or X-rays has been observed in current data (Abramowski et al. 2014). The spectrum of the GeV source 3FGL J1641.1−4619c is very soft (see Lemoine-Goumard et al. 2014), compared to the hard TeV spectrum detected by HESS (Abramowski et al. 2014) that suggests different origins for the GeV and TeV gamma-rays. Lau et al. (2017) have used observations of many molecular and atomic transitions towards HESS J1640−465 and HESS J1641−463 to gain an understanding of total gas distribution and mass to explore both hadronic and leptonic TeV emission scenarios. Lau et al. (2017) find that in a hadronic origin for the gamma-ray emission, the CR enhancement rates are ~10^3 and ~10^2 times the local solar value for HESS J1640−465 and HESS J1641−463, respectively. In the hadronic case, if HESS J1641−465 were produced by runaway protons from the SNR G338.3−0.0 and applying the diffusion distance estimate according to equation (3), protons of 100 TeV would take ~10 000 yr to travel from the SNR to the second TeV source if moving through the dense gas. In this case, however, we would expect the TeV gamma-rays to peak along with the density of molecular gas, which, as can be seen in Fig. 17, appears not to be the case. As outlined by Lau et al. (2017), and that can be seen in Table 2, in the highest density region, there are molecular cloud cores at different distances along the line of sight, which could allow for CR diffusion between them. This would allow for the CRs to diffuse faster, and using the diffuse gas parameters of Lau et al. (2017), we calculate that 100 TeV protons would take ~1600 yr to diffuse from SNR G338.3−0.0 to HESS J1641−463. As the age of SNR G338.3−0.0 has been estimated from 1–2 kyr up to 5–8 kyr, this would allow time for VHE CRs to travel from SNR

G338.3−0.0 to produce the TeV emission from HESS J1641−463, between dense cloud cores (as outlined in Lau et al. 2017).

4.3 HESS J1848−018

HESS J1848−018 is located towards the W43 star-forming region. No obvious counterparts for the TeV emission such as SNRs or energetic pulsars are seen towards HESS J1848−018 (Chaves et al. 2008). The high-mass stellar cluster W43 is offset from the centroid of the TeV emission within a giant molecular cloud with mass ~10^6 M$_\odot$ detected in both submillimetre wavelengths (Motte, Schilke & Lis 2003) and ^{13}CO (Jackson et al. 2006). This cluster contains the high-mass binary system, WR 121a, catalogued by van der Hucht (2001) and classified as a CWB by Anderson et al. (2011). Our observations (Fig. 19) reveal broad NH$_3$ emission lines in the giant molecular cloud as well as H$_2$O maser emission and H69α emission indicative of ongoing star formation and ionized gas towards WR 121a. The H69α emission traces the H II region G30.8−0.0 (Lester et al. 1985). The IRDC G030.97−00.14, catalogued by Rathborne, Jackson & Simon (2006), is seen towards the TeV centroid in Fig. 20, overlapping a gas clump detected in NH$_3$ (1,1) by our study. Spectra towards this gas clump are displayed on the LHS of Fig. 19, which show H$_2$O maser emission, indicative of active star formation. Due to the coincident IRDC, we suggest that this is an early star-forming region, slightly foreground to the W43 region that provides much of the extended, background 8 μm emission in Fig. 20, which is being absorbed by the cold, dense gas.

CWBs are expected to produce leptonic gamma-ray emission through IC scattering up to a few GeV (e.g. Pittard & Dougherty 2006; De Becker & Raucq 2013). Theoretical models suggest that, given a suitable environment, stellar winds that are ejected during the high-mass star evolution may also be able to accelerate hadrons as effectively as SNRs (see Farnier et al. 2011, and references therein). If the CWB WR 121a is indeed responsible for the TeV emission, then approximately 3 per cent of the kinetic power of the wind–wind collision (estimated to be ~10^{36} erg s^{-1} in the system WR140; Pittard & Dougherty 2006) is converted into TeV emission. This agrees with numerical simulations of relativistic collisionless shocks, which indicate that at least 10 per cent of energy is converted into relativistic particles downstream of the shock (Spitkovsky 2008).

Coincident with HESS J1848−018 are the *Fermi*-LAT source 3FGL J1848.4−0141 (Acero et al. 2015) and HAWC source 1HWCJ1849−017c (Abeysekara et al. 2016). While spectra of the HESS and HAWC sources have not been published, a continuous spectrum from *Fermi*-LAT energies up to tens of TeV (where HAWC is most sensitive) would point towards a hadronic origin to the gamma-rays, as leptonic sources are expected to cut off at lower energies. Further studies to determine the TeV morphology of HESS J1848−018 would be beneficial in determining whether the CWB WR 121a is a possible counterpart to the TeV emission. The cold, dense core detected by NH$_3$ observations in our study towards the IRDC G030.97−00.14 is within 2 arcmin of the TeV centroid and could provide a target for accelerated hadrons. A study of the morphology of more diffuse gas (i.e. that traced by ^{12}CO(1–0) and H I) is planned, and will give clues as to the origin of the TeV gamma-rays.

4.4 HESS J1626−490

The centroid of HESS J1626−490 is found within 0°.5 of the SNR G335.2 + 0.1 that has been noted as a possible source of accelerated
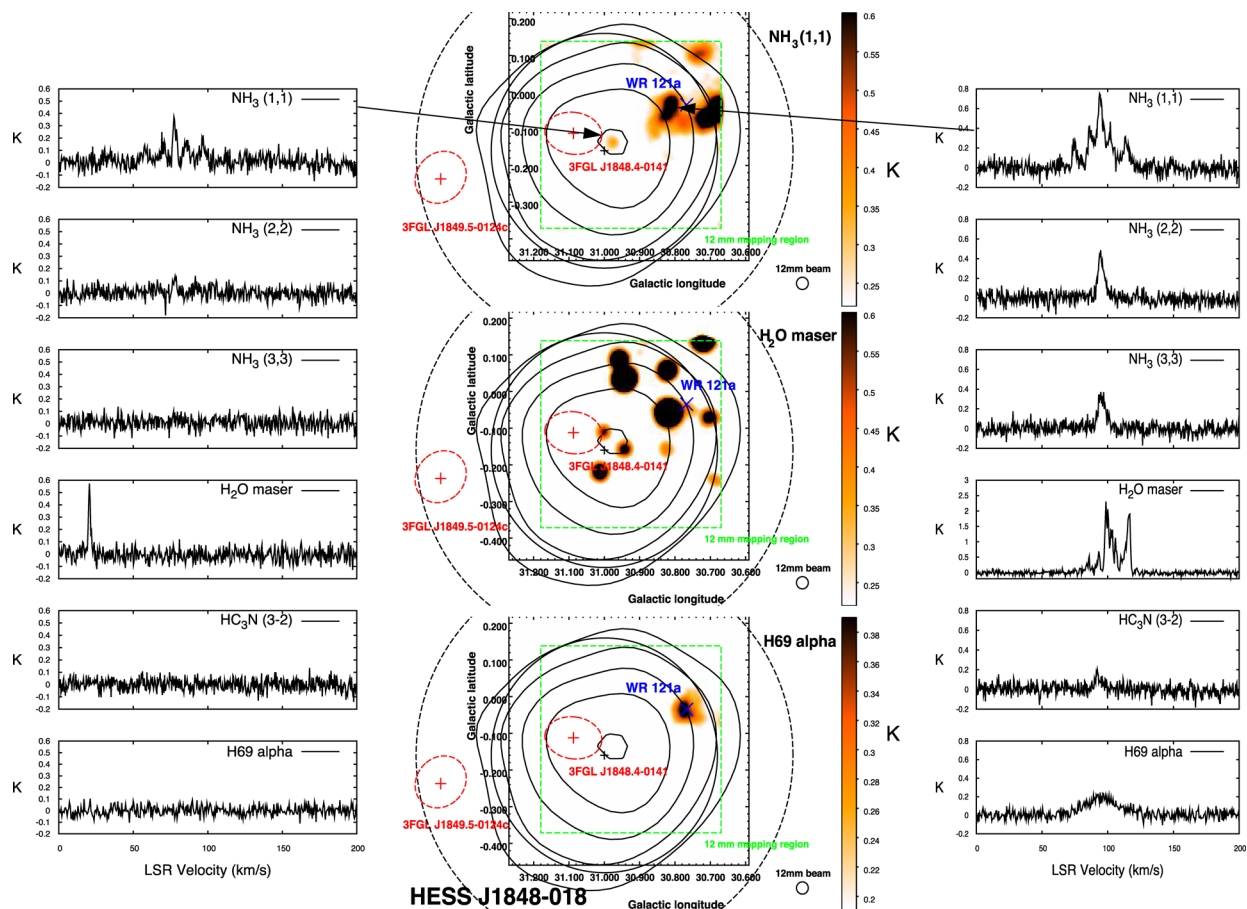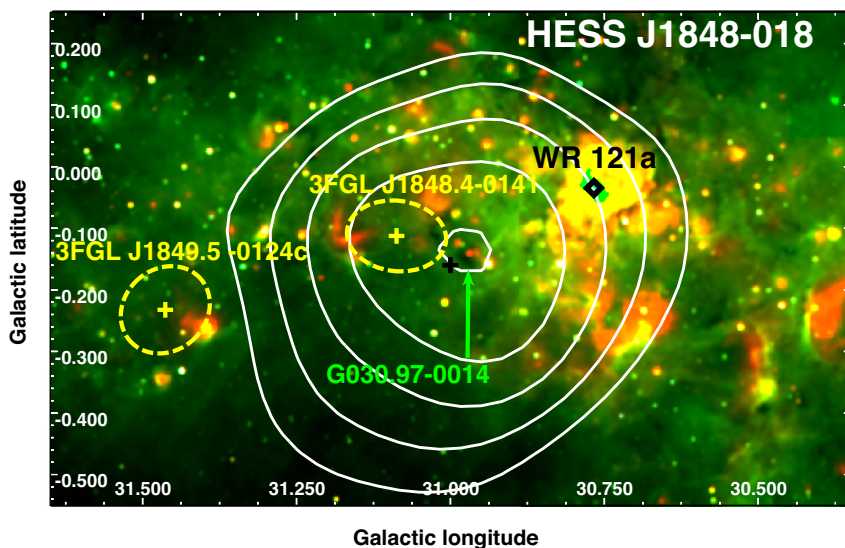
Figure 19. 12 mm peak pixel maps of molecular line emission towards the TeV source HESS J1848−018. The centroid position of TeV emission is indicated by a + and intrinsic size by the dashed circle. Peak brightness temperature images (as described in Fig. 15) of NH_3 (1,1), H_2O maser and H69α are shown. The mapping region is indicated by a green, dashed box and does not cover the extent of the TeV emission. The RHS spectra display emission in all molecular line transitions included in our study, indicating dense gas along with ongoing star formation and ionized gas towards the stellar cluster W43. The LHS spectra display emission in NH_3 (1,1) and NH_3 (2,2) indicating dense gas and H_2O emission indicating ongoing star formation towards the TeV emission centroid.

Figure 20. *Spitzer* GLIMPSE/MIPSGAL three-colour (RGB = 24/8/4.5 μm M Jy sr^{-1}) image of the region towards HESS J1848−018. The TeV emission is displayed as in Fig. 19. Notable features in this IR image include a saturation of 24 μm emission towards the W43 stellar cluster that contains CWB WR 121a as well as excess emission seen in all IR bands surrounding this region. The IRDC G030.97−00.14 is also seen, towards the TeV centroid, which matches the position of the gas clump traced by NH_3 (1,1) emission seen in Fig. 19.
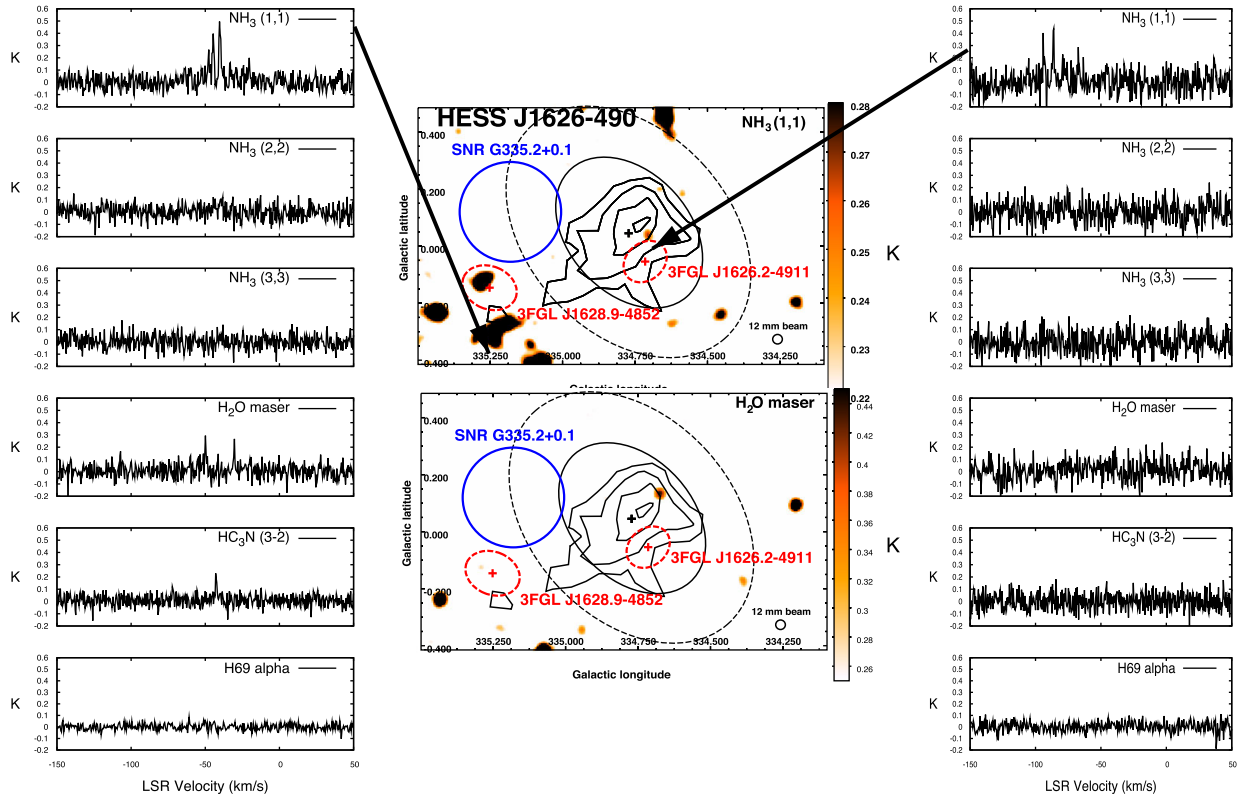
Figure 21. 12 mm peak pixel maps of molecular line emission towards the TeV source HESS J1626−490. TeV emission is indicted by black contours, *Fermi*-LAT sources are indicted by dashed, red ellipses, the SNR G335.2+0.1 is indicated by a blue circle and two H II regions are indicated by magenta ×s. Very little molecular emission towards this TeV source is detected in our study. A dense clump, traced by NH₃ (1,1) emission, is seen towards the TeV peak that also displays H₂O maser emission. Several molecular clumps, traced by emission from several transitions, are seen below the SNR G335.2+0.1 in this image.

particles responsible for the TeV emission (see Eger et al. 2011). An H I void is seen in Southern Galactic Plane Survey (SGPS; McClure-Griffiths et al. 2005) data between velocities of −24 and 9 km s^{-1} that is thought to correspond to the SNR (Eger et al. 2011). The GeV *Fermi*-LAT source 3FGL J1626.2−4911 is coincident with HESS J1626−490; however, the GeV and TeV spectra are not well matched and so the sources may not be associated. Our study reveals NH₃ (1,1) emission towards the TeV peak that can be seen in Fig. 21. The NH₃ (1,1) emission has a kinematic velocity of −86 km s^{-1}, giving implied kinematic distance solutions ∼5.5 kpc (near) and ∼8.6 kpc (far). The position of the molecular clump traced by NH₃ emission in our study corresponds to that of an IRDC that can be seen in Fig. 22. This indicates that it is foreground to the widespread IR emission. This IRDC, MSXDC G334.70+0.02, has been previously catalogued by Jackson et al. (2008). The widespread IR emission is assumed to originate from the complex containing the H II region G334.684−0.107, which has a distance of 12.8 kpc (Russeil et al. 2005). Both the near and far kinematic distances of the NH₃ clump are foreground to the H II region so this does not resolve the distance ambiguity. H I absorption towards the SNR G335.2+0.1 seen in H I data from SGPS (McClure-Griffiths et al. 2005) indicates an SNR distance between 5.9 and 12.4 kpc. Assuming that the SNR and NH₃ detected molecular core are at the same distance, we can assign the far distance of 8.7 kpc to the NH₃ (1,1) emission detected in this study. At a distance of 8.7 kpc, the distance for CR protons to travel from the SNR shell to the far side of HESS J1626−490 is 76 pc. Using equations (3) and (5) and assuming an average gas density of

1×10^2 cm^{-3} towards the TeV emission, 10^{13} eV CR protons would take ∼5300 yr to traverse this distance, and lower energy CRs would take a longer time. This would indicate a middle-aged or old SNR, at an age similar to other TeV emitting SNRs where a hadronic scenario is supported.

4.5 HESS J1804−216

HESS J1804−216 is seen towards a number of interesting features including SNR G8.7−0.1 (Odegard 1986) and several H II regions observed as part of catalogues (Wink, Altenhoff & Mezger 1982; Lockman, Pisano & Howard 1996; Kuchar & Clark 1997). The high spin-down power (2.2×10^{36} erg s^{-1}) PSR J1803−2137 offers a plausible PWN emission scenario for HESS J1804−216. However, the nature of the TeV source and its association with the X-ray sources found towards this object are still unclear (Kargaltsev, Pavlov & Garmire 2007). There is a 1720 MHz OH maser along the border of SNR G8.7−0.1. This maser signals a shock interaction between the SNR and dense clouds (Frail & Mitchell 1998); however, this maser is not coincident with the TeV emission as seen in Fig. 23. Several dense cloud clumps are seen in our study and are traced by the emission lines indicated in Table 2.

The dense gas seen in our study mainly surrounds the published extent of TeV emission. Thus, the morphology of the cool, dense gas supports a PWN scenario for the TeV emission. However, there is IR polyaromatic hydrocarbon (PAH) emission over the extent of the TeV emission, indicating that there is likely diffuse molecular material in this region not detected in our study. The lack of detected
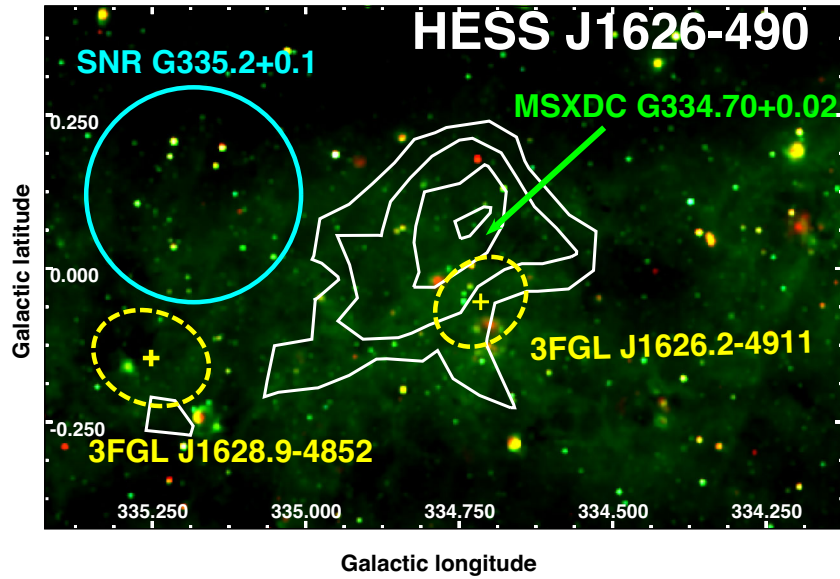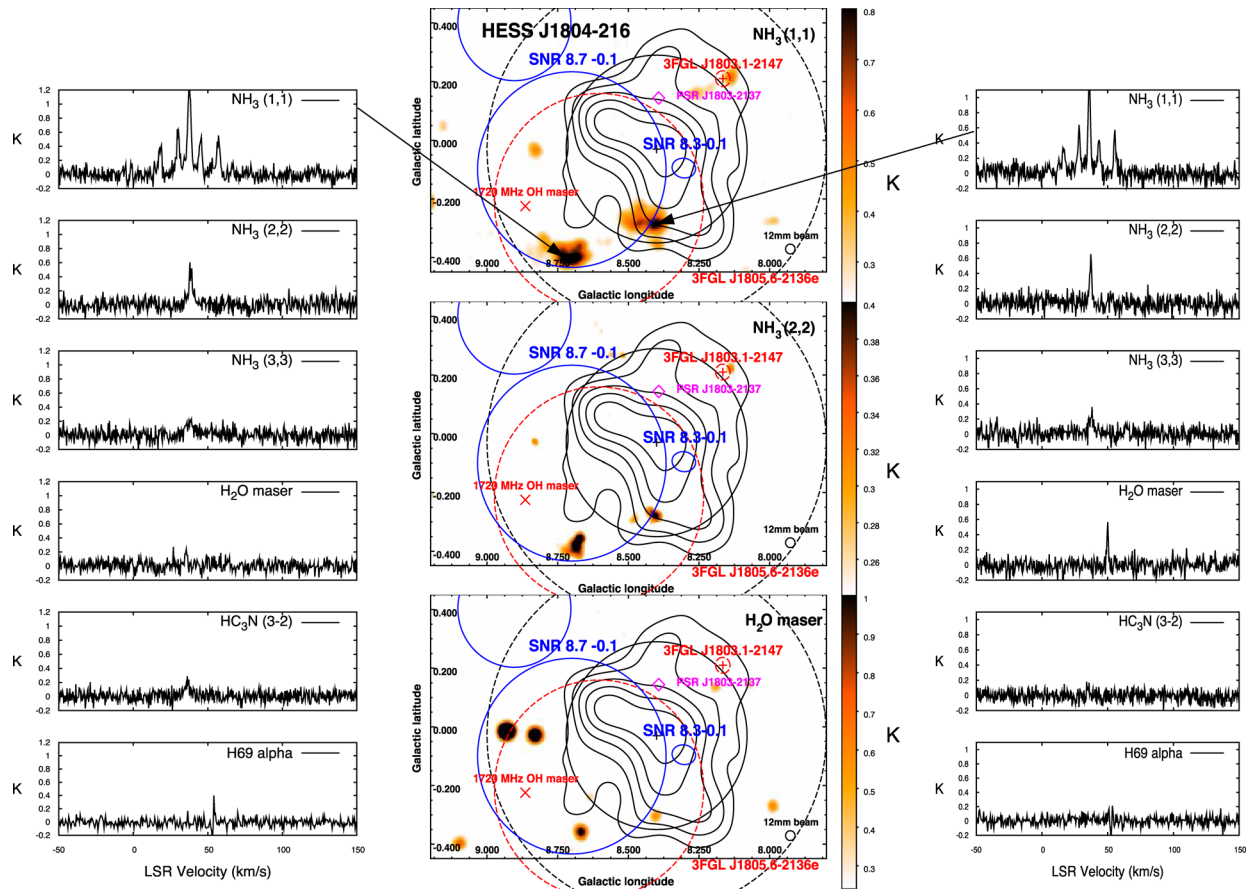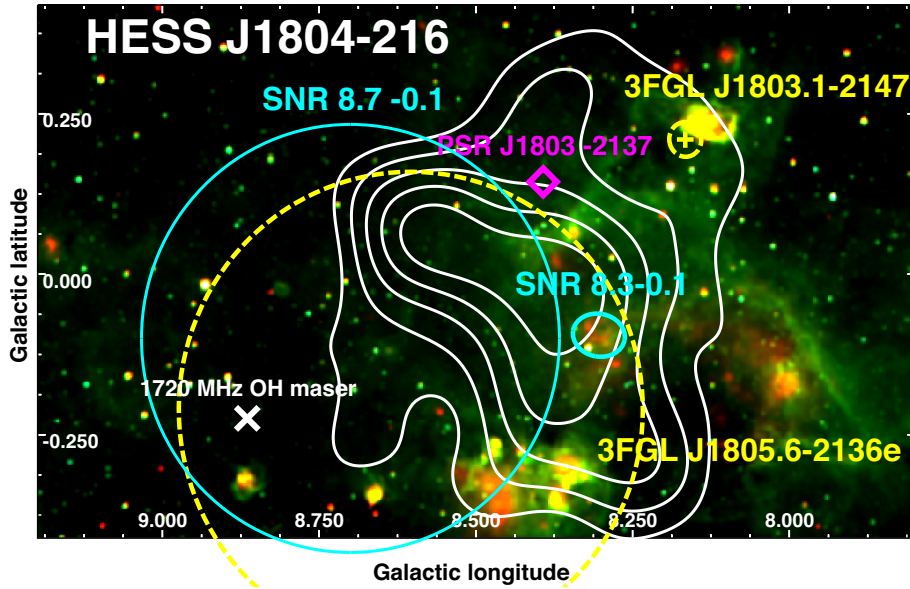
Figure 22. *Spitzer* GLIMPSE/MIPSGAL three-colour (RGB = 24/8/4.5 µm M Jy sr^{-1}) image of the region towards HESS J1626−490. TeV emission is indicated by white contours, *Fermi*-LAT sources are indicted by dashed, red ellipses and the SNR G335.2+0.1 is indicated by a cyan circle. Widespread 8 µm emission is seen, likely arising from polyaromatic hydrocarbon (PAH) emission. Several small 24 µm emission can be seen as yellow sources, which traces heated dust. The IRDC MSXDC G334.70+0.02 is indicated towards the TeV emission.

Figure 23. 12 mm peak pixel maps of molecular line emission towards the TeV source HESS J1804−216. TeV emission is indicted by black contours, *Fermi*-LAT sources are indicted by dashed, red ellipses and the SNR G8.7−0.1 is indicated by a blue circle. The molecular emission detected in our study is limited to the edges of TeV emission. All molecular clumps detected show H$_2$O and/or H69α emission.

Figure 24. *Spitzer* GLIMPSE/MIPSGAL three-colour (RGB = 24/8/4.5 μm M Jy sr^{-1}) image of the region towards HESS J1804−216. TeV emission is indicated by white contours, *Fermi*-LAT sources are indicted by dashed, red ellipses, the SNR G8.7−0.1 is indicated by a yellow, dashed circle, the pulsar PSR B1800−21 is indicated by a magenta square and H II regions are indicated by magenta ×s. Widespread 8 μm emission is seen, and numerous regions of heated dust (traced by 24 μm emission) are seen, especially along the outside edge of the SNR, possibly indicating triggered star formation.

12 mm emission towards the 1720 OH maser suggests that there are undetected molecular clouds in our study, since molecular material with a density ∼10^5 cm^{-3} is needed to produce 1720 MHz OH maser emission (Lockett, Gauthier & Elitzur 1999; Wardle 1999). This additional molecular material as well as atomic material traced by H I may provide enough target material for a hadronic origin of the TeV emission. Almost all NH$_3$ (1,1) emitting clumps near HESS J1804−216 display H$_2$O maser emission (as seen in Fig. 23).

HESS J1804−216 is one of the brightest unidentified TeV sources and so may provide the opportunity for improved angular resolution studies and energy-dependent morphology studies in TeV gamma-rays, potentially reducing confusion between counterparts at other wavelengths. Further studies of molecular gas, including tracers of warmer and more diffuse gas such as ^{12}CO(1−0), CS(1−0) and H I emission, should be undertaken in this region to account for more of the gas mass than is implied by our studies.

4.6 HESS J1729−345

HESS J1729−345 (aka HESS J1731−347 B) is offset from a TeV shell, HESS J1731−347 A (Abramowski et al. 2011b), and lies near the direction of the H II region G353.381−0.114 catalogued in Caswell & Haynes (1987) at a distance of >7.5 kpc that is not traced in this study. Previously, this H II region has been suggested as an indication for a molecular cloud complex, possible counterpart to HESS J1729−345. This molecular cloud complex is seen, traced by PAH emission in Fig. 26. In this work, a dense gas clump, traced with emission from the NH$_3$ (1,1) transition, is seen towards HESS J1729−345, at a velocity of −16 km s^{-1}. This gas feature is seen in Fig. 25 and also as an IRDC in Fig. 26. As this molecular cloud is seen as an IRDC, we can deduce that the NH$_3$ emission is foreground to the PAH emission which rules out the far kinematic distance solution, and tells us that the NH$_3$ cloud core is at the near kinematic distance solution of 3.8 kpc. This distance is within errors of a previous distance estimate of the SNR, based on its assumed connection to the compact H II region G353.42−0.37, of

3.2 ± 0.8 kpc (Tian et al. 2008). This is however foreground to a more recent SNR distance estimate of 5.2–6.2 kpc based on the assumption that the SNR is within the 3 kpc expanding arm (Fukuda et al. 2014). Further preliminary discussion about the distance of this source can be seen in Maxted et al. (2012), which details CS(1−0) emission.

If the molecular clump detected in this study was a counterpart to HESS J1729−345, the TeV emission could arise from π^0 decay resulting from p–p collisions between CRs accelerated in the SNR. We assume the SNR is at a distance of 3.8 kpc (Tian et al. 2008), along with the molecular clump towards HESS J1729−345 traced by NH$_3$ (1,1) in our study. At this distance and with an angular separation between the centre of the SNR and HESS J1729−345 of ∼0°.5, the protons would have travelled approximately 30 pc. Using the method outlined in Section 2, it would take ∼140 yr for a 10^{14} eV proton to diffuse from the SNR (HESS J1731−347) to HESS J1729−345 and ∼1400 yr for a 10^{12} eV proton. With an SNR age estimate of 27 000 yr (Tian et al. 2008), protons would have sufficient time to travel and interact with the molecular gas towards HESS J1729−345 and produce the TeV emission.

5 CONCLUSIONS/FURTHER WORK

The first large-scale systematic study of dense (>10^4 cm^{-3}) gas towards Galactic TeV sources has been completed. HOPS-equivalent coverage provides a good first look at distribution and dynamics of dense gas towards Galactic TeV sources. Knowledge about gas density profiles towards TeV sources allows for more robust studies of CR diffusion. Preliminary results suggest that 12 mm NH$_3$ inversion transitions, used to estimate NH$_3$ OPR, could be used to search for regions of dense gas with previous shock activity. With this first look, we have found dense gas counterparts to unidentified regions of TeV emission including HESS J1745−303B and HESS J1745−303C as well as HESS J1848−018 and HESS J1626−490, which indicate that it is likely that there is a hadronic component to these sources.
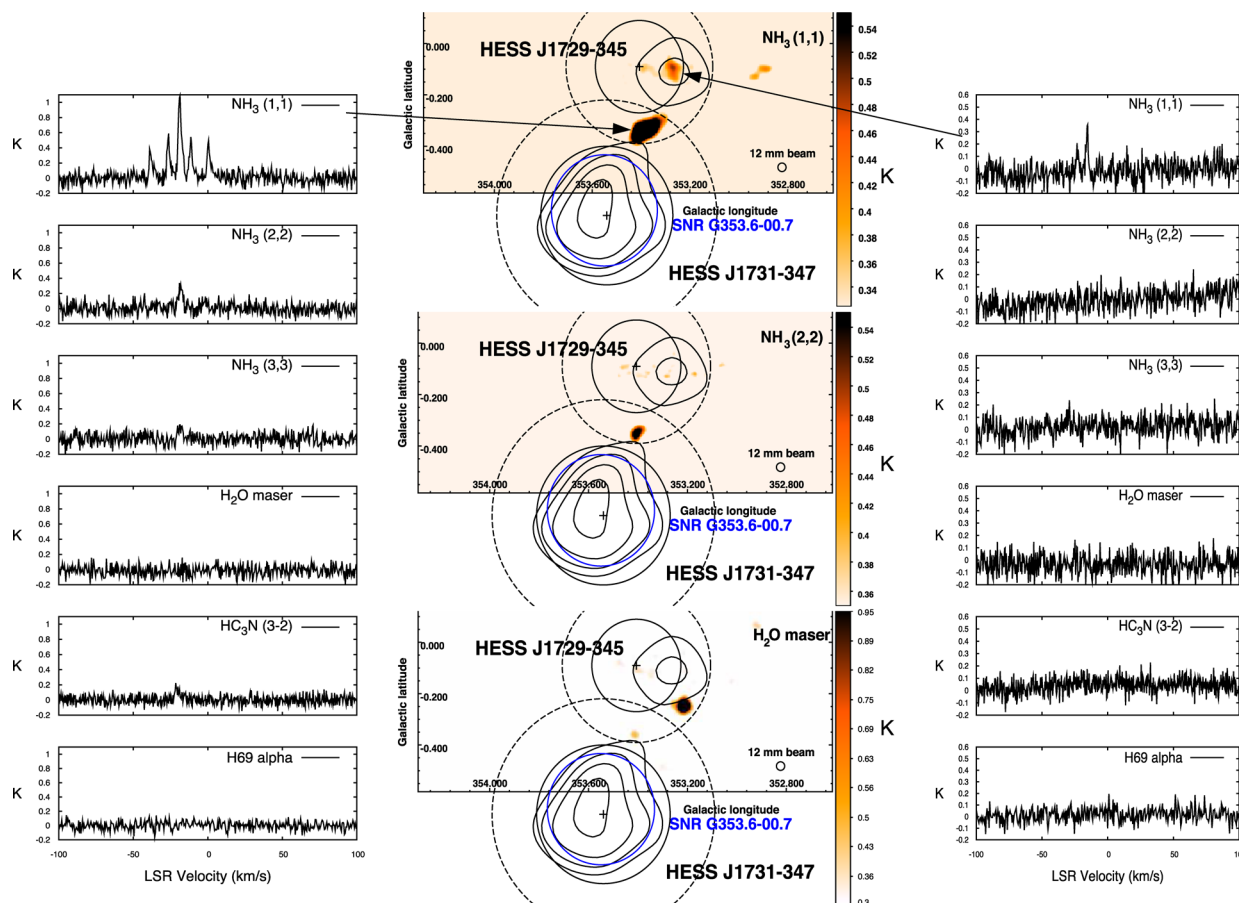
Figure 25. 12 mm peak pixel maps of molecular line emission towards the TeV sources HESS J1729−345 and HESS J1731−347. TeV emission is indicted by black contours, at the 4σ–7σ significance levels (from Abramowski et al. 2011b), and the defined 'towards' and 'adjacent' regions for HESS J1729−345 and HESS J1731−347 are represented by a black, thin, solid circle, and the area between this circle and a black, thin dashed circle, respectively. The edge of the 12 mm mapping region is indicated by the *x*-axis. Two molecular clumps can be seen, one towards the Galactic east from HESS J1729−345 at a velocity matching that identified for the SNR by Tian et al. (2008). The spectra for molecular transitions detected from this clump are seen on the RHS.
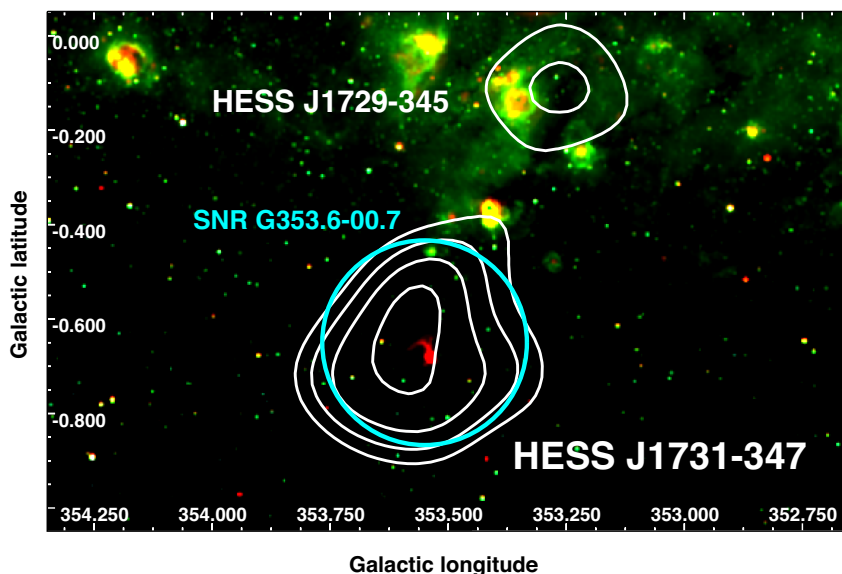
Figure 26. *Spitzer* GLIMPSE/MIPSGAL three-colour (RGB = 24/8/4.5 μm M Jy sr^{-1}) image of the region towards HESS J1729−345 and HESS J1731−347. TeV emission is indicated by white contours. Widespread 8 μm emission is seen towards HESS J1729−345 along with numerous regions of heated dust (traced by 24 μm emission). This emission is assumed to be background to the molecular emission traced by our study that is towards part of the IRDC, which can be seen extending from the SNR to HESS J1729−345.

Further observations of TeV sources showing dense gas overlap traced by the NH_3 (1,1) emission seen in the HOPS would be beneficial at millimetre wavelengths. Further 12 mm observations would provide more sensitivity to dense gas clumps traced by NH_3 emission. Observations at 7 mm to trace molecular transitions such as SiO(1–0), which traces shocked gas, and CS(1–0), which traces the denser features of gas clouds, will provide better understanding of the mechanisms producing the relativistic particles producing the TeV gamma-rays as well as understanding the kinematics of the densest parts of gas towards these TeV gamma-ray sources. Further 12 mm observations that include the NH_3 (4,4) and (5,5) transitions would be beneficial to estimate the NH_3 OPR in sources for which we have found an anomalous NH_3 (3,3)-to-(1,1) brightness temperature ratio.

In addition, studies of particle transport within individual TeV sources should include not only the dense gas described here, but also observations of moderately dense molecular gas, e.g. that traced by CO(1–0), and atomic gas, traced by H I, in order to understand density profiles of molecular clouds towards and adjacent to the TeV emission. The Mopra CO survey (Burton et al. 2013) provides a large-scale study for more diffuse gas towards Galactic TeV sources. With an angular resolution of 33 arcsec, and the inclusion of several isotopologues (including which help to trace a range of molecular gas densities, the Mopra CO survey will provide the most accurate large-scale look at molecular gas in the Milky Way for use with current and future gamma-ray data sets. The Mopra CO and HOPS angular resolution (33 arcsec and 1 arcmin, respectively) and the future CTA angular resolution (2–3 arcmin between 1 and 10 TeV) are comparable and have the ability to resolve molecular cloud cores. In addition, all of these observations will cover a significant portion of the Galactic plane allowing for improved morphological comparison studies, and robust statistical studies of molecular gas and TeV gamma-rays. These higher resolution gas surveys will also provide a necessary picture of the distribution of Galactic gas to be used for new gamma-ray emission templates needed for higher angular resolution gamma-ray observations. H I gas is also an important contribution to the target gas mass for CRs (e.g. Fukui et al. 2012). Quantifying the contribution from H I has been improved with recent studies of optically thick H I in the ISM (e.g. Fukui et al. 2015). The contribution of dark gas (both molecular and atomic) may also be important (e.g. Burton et al. 2015).

Currently, a robust statistical study of the overlap between Galactic TeV emission and star-forming regions is not possible due to confusion, sensitivity and uneven coverage. Recent observations of the Large Magellanic Cloud (H.E.S.S. Collaboration et al. 2015a) have shown that superbubbles are capable of producing TeV emission, and it is suspected that we will find similar Galactic environments. As the angular resolution of TeV instruments improves, specifically with CTA, to match that of molecular gas studies (such as HOPS and Mopra CO) and also the sensitivity of molecular gas observations improves, a much better understanding of the emission mechanisms and high-energy particle transport in Galactic star-forming regions will evolve.

REFERENCES

Abeysekara A. U. et al., 2016, ApJ, 817, 3
Abramowski A. et al., 2011a, A&A, 525, A46
Abramowski A. et al., 2011b, A&A, 531, A81
Abramowski A. et al., 2012, A&A, 537, A114
Abramowski A. et al., 2014, ApJ, 794, L1
Acero F. et al., 2015, ApJS, 218, 23
Aharonian F. et al., 2005, A&A, 439, 1013
Aharonian F. et al., 2006a, A&A, 449, 223
Aharonian F. et al., 2006b, A&A, 456, 245
Aharonian F. et al., 2006c, A&A, 457, 899
Aharonian F. et al., 2006d, ApJ, 636, 777
Aharonian F. et al., 2007, A&A, 472, 489
Aharonian F. et al., 2008a, A&A, 477, 353
Aharonian F. et al., 2008b, A&A, 481, 401
Aharonian F. et al., 2008c, A&A, 483, 509
Aharonian F. et al., 2008d, A&A, 484, 435
Aharonian F. et al., 2008e, A&A, 490, 685
Anderson G. E. et al., 2011, ApJ, 727, 105
Araudo A. T., Rodríguez L. F., 2012, in Aharonian F. A., Hofmann W., Rieger F. M., eds, AIP Conf. Ser. Vol. 1505, High Energy Gamma-ray Astronomy. Am. Inst. Phys., New York, p. 281
Bednarek W., Pabich J., 2011, A&A, 530, A49
Berezinskii V. S., Bulanov S. V., Dogiel V. A., Ptuskin V. S., 1990, Astrophysics of Cosmic Rays. North-Holland, Amsterdam
Bergin E. A., Alves J., Huard T., Lada C. J., 2002, ApJ, 570, L101
Blondin J. M., Chevalier R. A., Frierson D. M., 2001, ApJ, 563, 806
Bosch-Ramon V., Romero G. E., Araudo A. T., Paredes J. M., 2010, A&A, 511, A8
Braiding C. et al., 2015, PASA, 32, 20
Brand J., Blitz L., 1993, A&A, 275, 67
Burton M. G. et al., 2013, PASA, 30, 44
Burton M. G. et al., 2015, ApJ, 811, 13
Casse M., Paul J. A., 1980, ApJ, 237, 236
Caswell J. L., Haynes R. F., 1987, A&A, 171, 261
Chang C., Konopelko A., Cui W., 2008, ApJ, 682, 1177
Chaves R. C. G., Renaud M., Lemoine-Goumard M., Goret P., 2008, in Aharonian F. A., Hofmann W., Rieger F., eds, AIP Conf. Ser. Vol. 1085, High Energy Gamma-ray Astronomy. Am. Inst. Phys., New York, p. 372
Cheung A. C., Rank D. M., Townes C. H., Knowles S. H., Sullivan W. T., III, 1969, ApJ, 157, L13
Crutcher R. M., 1999, ApJ, 520, 706
De Becker M., Raucq F., 2013, A&A, 558, A28
de Oña Wilhelmi E., 2009, in Bastieri D., Rando R., eds, AIP Conf. Ser. Vol. 1112, Bridging the Gap Between GeV and TeV. Am. Inst. Phys., New York, p. 16
de Oña-Wilhelmi E. et al., 2013, Astropart. Phys., 43, 287
Deil C., Brun F., Carrigan S., Chaves R., Donath A., Gast H., Marrandon V., Terrier R., 2015, Prc. Sci., The H.E.S.S. Galactic Plane Survey. SISSA, Trieste, PoS(ICRC2015)773
Djannati-Ataï A., de Jager O. C., Terrier R., Gallant Y. A., Hoppe S., 2008, in International Cosmic Ray Conference. p. 823
Eger P., Rowell G., Kawamura A., Fukui Y., Rolland L., Stegmann C., 2011, A&A, 526, A82
Farnier C., Walter R., Leyder J.-C., 2011, A&A, 526, A57
Faure A., Hily-Blant P., Le Gal R., Rist C., Pineau des Forêts G., 2013, ApJ, 770, L2

Forster J. R., Caswell J. L., 2000, ApJ, 530, 371
Frail D. A., Mitchell G. F., 1998, ApJ, 508, 690
Fukuda T., Yoshiike S., Sano H., Torii K., Yamamoto H., Acero F., Fukui Y., 2014, ApJ, 788, 94
Fukui Y. et al., 2012, ApJ, 746, 82
Fukui Y., Torii K., Onishi T., Yamamoto H., Okamoto R., Hayakawa T., Tachihara K., Sano H., 2015, ApJ, 798, 6
Gabici S., Aharonian F. A., 2014, MNRAS, 445, L70
Gabici S., Aharonian F. A., Blasi P., 2007, Ap&SS, 309, 365
Gallant Y. A. et al., 2008, in Bassa C., Wang Z., Cumming A., Kaspi V. M., eds, AIP Conf. Ser. Vol. 983, 40 Years of Pulsars: Millisecond Pulsars, Magnetars and More. Am. Inst. Phys., New York, p. 195
Gotthelf E. V. et al., 2014, ApJ, 788, 155
Green A. J., 1999, in Taylor A. R., Landecker T. L., Joncas G., eds, ASP Conf. Ser. Vol. 168, New Perspectives on the Interstellar Medium. Astron. Soc. Pac., San Francisco, p. 43
Hayakawa T., Torii K., Enokiya R., Amano T., Fukui Y., 2012, PASJ, 64, 8
H.E.S.S. Collaboration et al., 2012, A&A, 548, A46
H.E.S.S. Collaboration et al., 2015a, Science, 347, 406
HESS Collaboration et al., 2015b, MNRAS, 446, 1163
Ho P. T. P., Townes C. H., 1983, ARA&A, 21, 239
Hofverberg P., Chaves R. C. G., Méhault J., de Naurois M., 2011, in Proc. 32nd Int. Cosmic Ray Conf., p. 248
Hofverberg P., 2010, Proc. Sci., Discovery of VHE gamma-rays from the vicinity of the shell-type SNR G318.2+0.1 with H.E.S.S. SISSA, Trieste, PoS(Texas 2010)196
Hoppe S., 2008, in Proc. 30th International Cosmic Ray Conference, p. 579
Inoue T., Inutsuka S.-i., 2012, ApJ, 759, 35
Inoue T., Yamazaki R., Inutsuka S.-i., Fukui Y., 2012, ApJ, 744, 71
Jackson J. M. et al., 2006, ApJS, 163, 145
Jackson J. M., Finn S. C., Rathborne J. M., Chambers E. T., Simon R., 2008, ApJ, 680, 349
Kargaltsev O., Pavlov G. G., Garmire G. P., 2007, ApJ, 670, 643
Kothes R., Dougherty S. M., 2007, A&A, 468, 993
Kuchar T. A., Clark F. O., 1997, ApJ, 488, 224
Lau J. C. et al., 2017, MNRAS, 464, 3757
Lemoine-Goumard M., Grondin M.-H., Acero F., Ballet J., Laffon H., Reposeur T., 2014, ApJ, 794, L16
Lester D. F., Dinerstein H. L., Werner M. W., Harvey P. M., Evans N. J., II, Brown R. L., 1985, ApJ, 296, 565
Lockett P., Gauthier E., Elitzur M., 1999, ApJ, 511, 235
Lockman F. J., Pisano D. J., Howard G. J., 1996, ApJ, 472, 173
McClure-Griffiths N. M., Dickey J. M., Gaensler B. M., Green A. J., Haverkorn M., Strasser S., 2005, ApJS, 158, 178
Manchester R. N., Hobbs G. B., Teoh A., Hobbs M., 2005, AJ, 129, 1993
Maret S., Faure A., Scifoni E., Wiesenfeld L., 2009, MNRAS, 399, 425
Mattana F. et al., 2009, ApJ, 694, 12
Maxted N. I. et al., 2012, MNRAS, 422, 2230
Maxted N. I., de Wilt P., Rowell G. P., Nicholas B. P., Burton M. G., Walsh A., Fukui Y., Kawamura A., 2016, MNRAS, 462, 532
Motte F., Schilke P., Lis D. C., 2003, ApJ, 582, 277
Nicholas B., Rowell G., Burton M. G., Walsh A., Fukui Y., Kawamura A., Longmore S., Keto E., 2011, MNRAS, 411, 1367
Nicholas B. P., Rowell G., Burton M. G., Walsh A. J., Fukui Y., Kawamura A., Maxted N. I., 2012, MNRAS, 419, 251

Odegard N., 1986, AJ, 92, 1372
Pedaletti G., de Oña Wilhelmi E., Torres D. F., 2014, A&A, 565, A118
Pittard J. M., Dougherty S. M., 2006, MNRAS, 372, 801
Pühlhofer G. et al., 2015, preprint (arXiv:1509.03872)
Purcell C. R. et al., 2012, MNRAS, 426, 1972
Rathborne J. M., Jackson J. M., Simon R., 2006, ApJ, 641, 389
Reitberger K., Reimer A., Reimer O., Takahashi H., 2015, A&A, 577, A100
Renaud M., Goret P., Chaves R. C. G., 2008, in Aharonian F. A., Hofmann W., Rieger F., eds, AIP Conf. Ser. Vol. 1085, High Energy Gamma-ray Astronomy. Am. Inst. Phys., New York, p. 281
Rowell G., De Naurois M., Djannati-Ataï S., Gallant Y., H. E. S. S. Collaboration, 2012, in Aharonian F. A., Hofmann W., Rieger F. M., eds, AIP Conf. Ser. Vol. 1505, High Energy Gamma-ray Astronomy. Am. Inst. Phys., New York, p. 273
Russeil D., Adami C., Amram P., Le Coarer E., Georgelin Y. M., Marcelin M., Parker Q., 2005, A&A, 429, 497
Sheidaei F., Djannati-Ataï A., Gast H., 2011, in Proc. 32nd International Cosmic Ray Conference. p. 244
Spitkovsky A., 2008, ApJ, 682, L5
Sugizaki M., Mitsuda K., Kaneda H., Matsuzaki K., Yamauchi S., Koyama K., 2001, ApJS, 134, 77
Suzuki H., Yamamoto S., Ohishi M., Kaifu N., Ishikawa S.-I., Hirahara Y., Takano S., 1992, ApJ, 392, 551
Tafalla M., Myers P. C., Caselli P., Walmsley C. M., Comito C., 2002, ApJ, 569, 815
Tian W. W., Leahy D. A., Haverkorn M., Jiang B., 2008, ApJ, 679, L85
Tibolla O., Komin N., Kosack K., Naumann-Godo M., 2008, in Aharonian F. A., Hofmann W., Rieger F., eds, AIP Conf. Ser. Vol. 1085, High Energy Gamma-ray Astronomy. Am. Inst. Phys., New York, p. 249
Uchida K. I., Morris M., Bally J., Pound M., Yusef-Zadeh F., 1992, ApJ, 398, 128
Umemoto T., Mikami H., Yamamoto S., Hirano N., 1999, ApJ, 525, L105
Ungerechts H., Winnewisser G., Walmsley C. M., 1986, A&A, 157, 207
Urquhart J. S. et al., 2010, PASA, 27, 321
van der Hucht K. A., 2001, New Astron. Rev., 45, 135
Voisin F., Rowell G., Burton M. G., Walsh A., Fukui Y., Aharonian F., 2016, MNRAS, 458, 2813
Walmsley C. M., Ungerechts H., 1983, A&A, 122, 164
Walsh A. J. et al., 2011, MNRAS, 416, 1764
Wardle M., 1999, ApJ, 525, L101
Whiteoak J. B. Z., Green A. J., 1996, A&AS, 118, 329
Wink J. E., Altenhoff W. J., Mezger P. G., 1982, A&A, 108, 227
Zirakashvili V. N., Aharonian F. A., 2010, ApJ, 708, 965

SUPPORTING INFORMATION

Supplementary data are available at *MNRAS* online.

Please note: Oxford University Press is not responsible for the content or functionality of any supporting materials supplied by the authors. Any queries (other than missing material) should be directed to the corresponding author for the article.

This paper has been typeset from a TEX/LATEX file prepared by the author.